

# Anomalous gauge couplings of the Higgs boson at high energy photon colliders

Tao Han<sup>1,3,4</sup>, Yu-Ping Kuang<sup>2,3</sup>, and Bin Zhang<sup>3,1</sup>

<sup>1</sup>*Department of Physics, University of Wisconsin, Madison, WI 53706, U.S.A.\**

<sup>2</sup>*CCAST (World Laboratory), P.O. Box 8730, Beijing 100080, P.R. China*

<sup>3</sup>*Center for High Energy Physics, Tsinghua University, Beijing 100084, P.R. China<sup>†</sup>*

<sup>4</sup>*Institute of Theoretical Physics, Academia Sinica, Beijing 100080, P.R. China*

## Abstract

We study the sensitivity of testing the anomalous gauge couplings  $g_{HVV}$ 's of the Higgs boson in the formulation of linearly realized gauge symmetry via the processes  $\gamma\gamma \rightarrow ZZ$  and  $\gamma\gamma \rightarrow WWWW$  at polarized and unpolarized photon colliders based on  $e^+e^-$  linear colliders of c.m. energies 500 GeV, 1 TeV, and 3 TeV. Signals beyond the standard model (SM) and SM backgrounds are carefully studied. We propose certain kinematic cuts to suppress the standard model backgrounds. For an integrated luminosity of  $1 \text{ ab}^{-1}$ , we show that (a)  $\gamma\gamma \rightarrow ZZ$  can provide a test of  $g_{H\gamma\gamma}$  to the  $3\sigma$  sensitivity of  $O(10^{-3} - 10^{-2}) \text{ TeV}^{-1}$  at a 500 GeV ILC, and  $O(10^{-3}) \text{ TeV}^{-1}$  at a 1 TeV ILC and a 3 TeV CLIC, and (b)  $\gamma\gamma \rightarrow WWWW$  at a 3 TeV CLIC can test all the anomalous couplings  $g_{HVV}$ 's to the  $3\sigma$  sensitivity of  $O(10^{-3} - 10^{-2}) \text{ TeV}^{-1}$ .

PACS number(s): 12.60.Fr, 13.88.+e, 14.80.Cp

---

\* Email address: than@physics.wis.edu.

<sup>†</sup> Mailing address for Yu-Ping Kuang and Bin Zhang. Email: ypkuang@mail.tsinghua.edu.cn, zb@mail.tsinghua.edu.cn.

## I. INTRODUCTION

Probing the mechanism of electroweak symmetry breaking (EWSB) is one of the most important tasks at TeV-scale colliders. The direct search in the CERN LEP experiments for the Higgs boson, which is related to EWSB and mass generation as predicted in the standard model (SM), sets a lower bound on its mass  $m_H > 114.4$  GeV [1]. The precision electroweak data favors a light Higgs boson with a mass  $m_H \leq 186$  GeV at 95% C.L. [1, 2]. It has been shown that convincing evidence for a SM-like Higgs boson would be discovered at the CERN Large Hadron Collider (LHC) [3] and be studied in great detail at  $e^+e^-$  International linear colliders (ILC) [4]. Once a Higgs boson is found at TeV-scale colliders, it is of fundamental importance to check if the Higgs boson is SM-like by studying its couplings to the SM particles. Primarily due to the “naturalness” argument [5] for a light Higgs boson, it is widely believed that physics beyond the SM must exist at a scale  $\Lambda$  near the order of TeV. In particular, if there are no new light particles observed other than the Higgs boson in the next generation collider experiments, it is even more pressing to determine the Higgs boson couplings as accurately as possible to seek for hints for new physics beyond the SM.

To extend the structure of the SM in a model-independent approach, it is customary to formulate new physics effects by linearly realizing the gauge symmetry [6, 7]. After integrating out heavy degrees of freedom at the scale  $\Lambda$ , the leading effects at low energies can be parameterized by the effective interactions

$$\mathcal{L}_{\text{eff}} = \sum_n \frac{f_n}{\Lambda^2} \mathcal{O}_n, \quad (1)$$

where  $f_n$ ’s are dimensionless “anomalous couplings”, and  $\mathcal{O}_n$  the gauge-invariant dimension-6 operators, constructed from the SM fields. If  $\Lambda$  appropriately parameterizes the new physics scale (such as the mass of the next resonance), then one would expect  $f_n$ ’s to be of the order of unity. The anomalous couplings of the Higgs boson and gauge bosons are of special interest since they may be directly related to the mechanism of EWSB. Theoretical studies of testing the anomalous gauge couplings of the Higgs boson already exist in the literature for the LHC [8–12], and for the ILC [13–15]. In this paper, we extend the literature by performing a systematic study of testing the anomalous gauge couplings of the Higgs boson at polarized and unpolarized photon colliders based on  $e^+e^-$  linear colliders of various energies. We consider the processes

$$\gamma\gamma \rightarrow ZZ, \quad \gamma\gamma \rightarrow WWWW.$$

We show that a photon collider can be more beneficial, and the sensitivity to the couplings can be

improved over the current results from other colliders.

This paper is organized as follows. In Sec. II, we review the operators for the anomalous gauge couplings of the Higgs boson and present the current constraints on them. In Sec. III, we summarize the backscattered photon spectrum adopted in our calculations, and give a brief sketch for calculating the cross sections at the polarized and unpolarized photon colliders based on the  $e^+e^-$  linear colliders. Secs. IV and V are the studies on the  $\gamma\gamma \rightarrow ZZ$  and  $\gamma\gamma \rightarrow WWWW$  processes, respectively. The summary of the results is given in Sec. VI.

## II. ANOMALOUS GAUGE COUPLINGS OF THE HIGGS BOSON

In the formulation of linearly realized gauge symmetry, the  $C$  and  $P$  conserving dimension-6 effective operators of our current interests involving the  $SU(2)$  gauge field  $W_\mu^i$ , the  $U(1)$  gauge field  $B_\mu$  as well as a Higgs doublet  $\Phi$  are given by [6, 7, 15]

$$\mathcal{O}_{BW} = \Phi^\dagger \hat{B}_{\mu\nu} \hat{W}^{\mu\nu} \Phi, \quad \mathcal{O}_{\Phi,1} = (D_\mu \Phi)^\dagger \Phi^\dagger \Phi (D^\mu \Phi), \quad (2)$$

$$\mathcal{O}_{\Phi,2} = \frac{1}{2} \partial^\mu (\Phi^\dagger \Phi) \partial_\mu (\Phi^\dagger \Phi), \quad \mathcal{O}_{\Phi,3} = \frac{1}{3} (\Phi^\dagger \Phi)^3, \quad (3)$$

$$\begin{aligned} \mathcal{O}_W &= (D_\mu \Phi)^\dagger \hat{W}^{\mu\nu} (D_\nu \Phi), & \mathcal{O}_B &= (D_\mu \Phi)^\dagger \hat{B}^{\mu\nu} (D_\nu \Phi), \\ \mathcal{O}_{WW} &= \Phi^\dagger \hat{W}_{\mu\nu} \hat{W}^{\mu\nu} \Phi, & \mathcal{O}_{BB} &= \Phi^\dagger \hat{B}_{\mu\nu} \hat{B}^{\mu\nu} \Phi, \end{aligned} \quad (4)$$

where  $\hat{B}_{\mu\nu}$  and  $\hat{W}_{\mu\nu}$  stand for

$$\hat{B}_{\mu\nu} = i \frac{g'}{2} B_{\mu\nu}, \quad \hat{W}_{\mu\nu} = i \frac{g}{2} \sigma^a W_{\mu\nu}^a,$$

in which  $g$  and  $g'$  are the  $SU(2)$  and  $U(1)$  gauge couplings, respectively.

Precision electroweak data and the measurements of the triple-gauge-boson couplings give considerable constraints on some of the anomalous couplings  $f_n/\Lambda^2$  in Eq. (1) [12, 14, 15]. For instance, the oblique correction parameters  $S$  and  $T$  [16] give rise to rather stringent constraints on the anomalous coupling constants  $f_{BW}$  and  $f_{\Phi,1}$  in Eq. (2) [12, 15]. The  $1\sigma$  and  $2\sigma$  contours for  $f_{BW}$  and  $f_{\Phi,1}$  from the updated experimental values of  $S$  and  $T$  are given in Ref. [12]. Assuming either  $f_{BW}$  or  $f_{\Phi,1}$  dominance, the  $2\sigma$  constraints obtained are quite strong [12],

$$-0.07 < \frac{f_{BW}}{(\Lambda/\text{TeV})^2} < 0.04, \quad -0.02 < \frac{f_{\Phi,1}}{(\Lambda/\text{TeV})^2} < 0.02.$$

The next two operators in Eq. (3) are purely Higgs boson self-interactions, and lead to corrections to the Higgs triple and quartic vertices. They have been dedicatedly studied in [14] at linear colliders and

we will not pursue them further. However, the present experimental observables are not sensitive to the four anomalous coupling operators  $O_W$ ,  $O_{WW}$ ,  $O_B$  and  $O_{BB}$  (with anomalous coupling constants  $f_W/\Lambda^2$ ,  $f_{WW}/\Lambda^2$ ,  $f_B/\Lambda^2$  and  $f_{BB}/\Lambda^2$ ) in Eq. (4). The constraints from the existing experiments and the requirement of unitarity of the  $S$  matrix element on these four anomalous coupling constants are rather weak. We summarize the above constraints on those four anomalous couplings in TABLE I. The results are obtained by assuming only one anomalous coupling exists each time.

TABLE I: Current  $2\sigma$  constraints on  $f_n/\Lambda^2$  from existing studies. The results are obtained by assuming only one anomalous coupling exists each time.

Constraints from	$f_n/\Lambda^2$ in $\text{TeV}^{-2}$
Precision EW fit [12]:	$-6 \leq \frac{f_W}{\Lambda^2} \leq 5$
	$4.2 \leq \frac{f_B}{\Lambda^2} \leq 2.0$
	$-5.0 \leq \frac{f_{WW}}{\Lambda^2} \leq 5.6$
	$17 \leq \frac{f_{BB}}{\Lambda^2} \leq 20$
Triple gauge coupling [15]	$-31 \leq \frac{f_W + f_B}{\Lambda^2} \leq 68$
LEP2 Higgs searches [8]:	$-7.5 \leq \frac{f_{WW(BB)}}{\Lambda^2} \leq 18$
Unitarity (at $\sqrt{s}=2$ TeV) [17]:	$ \frac{f_B}{\Lambda^2}  \leq 24.5; \quad  \frac{f_W}{\Lambda^2}  \leq 7.8$
	$-160 \leq  \frac{f_{BB}}{\Lambda^2}  \leq 197; \quad  \frac{f_{WW}}{\Lambda^2}  \leq 39.2$

It is perhaps more intuitive to express the new operators in terms of couplings of the explicit physical component fields. Taking into account the mixing between  $W_\mu^3$  and  $B_\mu$ , the effective couplings of the Higgs boson  $H$  and the electroweak gauge bosons  $V$  ( $V = \gamma, W^\pm, Z$ ) in Eqs. (1) and (4) can be cast into [15]

$$\begin{aligned}
\mathcal{L}_{\text{eff}}^H = & g_{H\gamma\gamma} H A_{\mu\nu} A^{\mu\nu} + g_{HZ\gamma}^{(1)} A_{\mu\nu} Z^\mu \partial^\nu H + g_{HZ\gamma}^{(2)} H A_{\mu\nu} Z^{\mu\nu} + g_{HZZ}^{(1)} Z_{\mu\nu} Z^\mu \partial^\nu H \\
& + g_{HZZ}^{(2)} H Z_{\mu\nu} Z^{\mu\nu} + g_{HWW}^{(1)} (W_{\mu\nu}^+ W^{-\mu} \partial^\nu H + \text{h.c.}) + g_{HWW}^{(2)} H W_{\mu\nu}^+ W^{-\mu\nu}, \quad (5)
\end{aligned}$$

where the anomalous couplings  $g_{HVV}$ 's (of dimension  $-1$ ) are related to those Lagrangian parameters

$f_n$ 's by

$$\begin{aligned}
g_{H\gamma\gamma} &= -\alpha \frac{s^2(f_{BB} + f_{WW})}{2}, \\
g_{HZ\gamma}^{(1)} &= \alpha \frac{s(f_W - f_B)}{2c}, & g_{HZ\gamma}^{(2)} &= \alpha \frac{s[s^2 f_{BB} - c^2 f_{WW}]}{c}, \\
g_{HZZ}^{(1)} &= \alpha \frac{c^2 f_W + s^2 f_B}{2c^2}, & g_{HZZ}^{(2)} &= -\alpha \frac{s^4 f_{BB} + c^4 f_{WW}}{2c^2}, \\
g_{HWW}^{(1)} &= \alpha \frac{f_W}{2}, & g_{HWW}^{(2)} &= -\alpha f_{WW},
\end{aligned} \tag{6}$$

with the weak mixing  $s \equiv \sin \theta_W$ ,  $c \equiv \cos \theta_W$  and  $\alpha = gM_W/\Lambda^2 \approx 0.053 \text{ TeV}^{-1} \approx 1/(19 \text{ TeV})$ . Roughly speaking, an order unity coupling of  $f_n$  translates to  $g_{HVV}^{(i)} \sim 1/(20 \text{ TeV}) = 0.05 \text{ TeV}^{-1}$ .

Since new physics responsible for the mechanism of the EWSB is more likely to show up with the Higgs couplings to gauge bosons, these couplings should be tested as thoroughly as possible at future high energy colliders [8–15]. At the LHC, it is shown in Ref. [12] that the most sensitive constraints on  $f_W/\Lambda^2$  and  $f_{WW}/\Lambda^2$  will be from the measurement of the gauge-boson scattering  $W^+W^+ \rightarrow W^+W^+$ . The  $2\sigma$  level constraints obtained on these two anomalous couplings are

$$-1.4 \text{ TeV}^{-2} < f_W/\Lambda^2 < 1.2 \text{ TeV}^{-2}, \quad \text{and} \quad 2.2 \text{ TeV}^{-2} \leq f_{WW}/\Lambda^2 < 2.2 \text{ TeV}^{-2}, \tag{7}$$

which may reach the parameter regime sensitive to TeV-scale new physics. Those processes are insensitive to  $f_B/\Lambda^2$  and  $f_{BB}/\Lambda^2$  however [12]. At  $e^+e^-$  linear colliders on the other hand, the anomalous couplings  $g_{HZZ}^{(1)}$  and  $g_{HZZ}^{(2)}$  can be constrained at the  $2\sigma$  sensitivity to  $(10^{-3} - 10^{-2}) \text{ TeV}^{-1}$  from the Higgs-strahlung process  $e^+e^- \rightarrow Z^* \rightarrow ZH$  [13].

We will see in the later sections that, at photon colliders, the sensitivities to probe those couplings can be improved.

### III. BACKSCATTERING PHOTON SPECTRUM AND GAUGE-BOSON PRODUCTION

By means of laser backscattering, a photon collider [18, 19] can be built on an  $e^+e^-$  linear collider. Let  $m_e$  and  $E_e$  be the incident electron mass and energy, respectively;  $\omega_0$  and  $\omega$  be the laser photon and the backscattered photon energies, respectively;  $\sqrt{s}$  be the  $e^+e^-$  center-of-mass energy;  $\sqrt{\hat{s}}$  be the center-of-mass energy of the backscattered photon; and  $M_V$  be the mass of the produced weak gauge boson. For an unpolarized photon collider, the cross section  $\sigma(s)$  for the production of  $2n$  weak gauge bosons at the photon collider can be obtained by convoluting the subprocess cross section  $\sigma(\hat{s})$  with the photon luminosity at an  $e^+e^-$  linear collider

$$\sigma(s) = \int_{2nM_V/\sqrt{\hat{s}}}^{x_{max}} dz \frac{dL_{\gamma\gamma}}{dz} \sigma(\hat{s}), \quad \hat{s} = z^2 s, \tag{8}$$

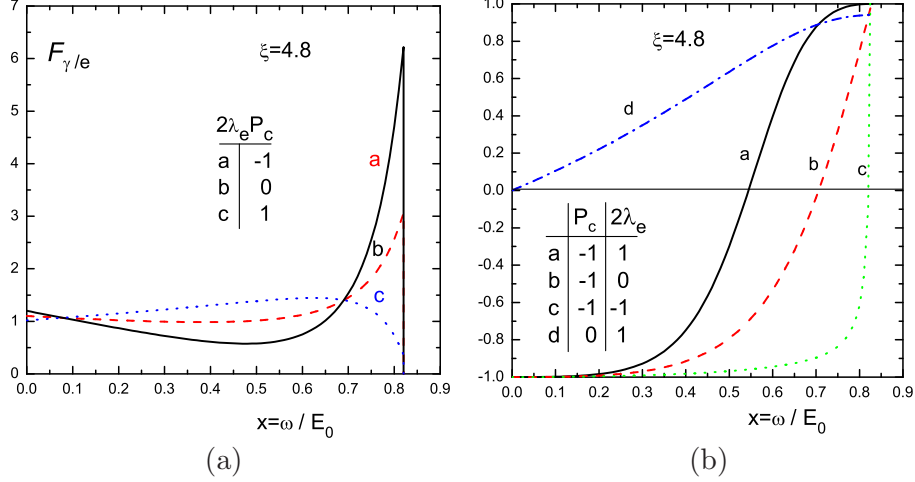


FIG. 1: (a) Photon energy distribution and (b) averaged helicity distributions with  $x = \omega / E_e$  for various values of  $2\lambda_e P_c$  at polarized photon colliders (based on the formulas given in Ref. [21]).

where  $x_{max} = \omega_{max} / E_e$ , and  $dL_{\gamma\gamma} / dz$  is the photon luminosity defined as

$$\frac{dL_{\gamma\gamma}}{dz} = 2z \int_{z^2/x_{max}}^{x_{max}} \frac{dx}{x} F_{\gamma/e}(x) F_{\gamma/e}(z^2/x). \quad (9)$$

The energy spectrum  $F_{\gamma/e}(x)$  of the backscattered photon at an unpolarized photon collider is given by [18]

$$F_{\gamma/e}(x) = \frac{1}{D(\xi)} \left[ 1 - x + \frac{1}{1-x} - \frac{4x}{\xi(1-x)} + \frac{4x^2}{\xi^2(1-x)^2} \right], \quad (10)$$

$$D(\xi) = \left( 1 - \frac{4}{\xi} - \frac{8}{\xi^2} \right) \ln(1 + \xi) + \frac{1}{2} + \frac{8}{\xi} - \frac{1}{2(1 + \xi)^2}, \quad (11)$$

where  $\xi = 4E_e\omega_0/m_e^2$ , and  $x = \omega/E_e$  is the energy fraction carried by the backscattered photon.  $F_{\gamma/e}(x)$  vanishes for  $x > x_{max} = \omega_{max}/E_e = \xi/(1 + \xi)$ . In order to avoid the creation of  $e^+e^-$  pairs by the interaction of the incident and backscattered photons, we require  $\omega_0 x_{max} \leq m_e^2/E_e$  which implies  $\xi \leq 2 + 2\sqrt{2} \approx 4.8$ . For the choice of  $\xi = 4.8$ , we obtain

$$x_{max} \approx 0.83, \quad D(\xi) \approx 1.8. \quad (12)$$

We will take these values for the unpolarized spectrum in our numerical calculations unless stated otherwise.

As for a polarized photon collider, let  $P_c$  be the polarization of the initial laser,  $\lambda_e$  the polarization of the electron beam, the energy spectrum of the backscattered photon beam is

$$F_{\gamma/e}(x, \lambda_e, P_c) = \frac{1}{D(\xi, \lambda_e, P_c)} \left[ 1 - x + \frac{1}{1-x} - \frac{4x}{\xi(1-x)} + \frac{4x^2}{\xi^2(1-x)^2} \right]$$

$$- 2\lambda_e P_c \left( \frac{x}{1-x} - \frac{2x^2}{(1-x)^2 \xi} \right) (2-x) \Big], \quad (13)$$

$$\begin{aligned} D(\xi, \lambda_e, P_c) = & \left(1 - \frac{4}{\xi} - \frac{8}{\xi^2}\right) \ln(1+\xi) + \frac{1}{2} + \frac{8}{\xi} - \frac{1}{2(1+\xi)^2} \\ & + 2\lambda_e P_c \left[ (1+2/\xi) \ln(\xi+1) - 5/2 + 1/(\xi+1) - \frac{1}{2(\xi+1)^2} \right]. \end{aligned} \quad (14)$$

It is shown in Ref. [20] that the energy spectrum of the colliding photons peaks in a narrow region near the high energy end (80% of the electron energy) if  $2\lambda_e P_c = -1$ , as demonstrated in Fig. 1(a) by the solid curve. For comparison, the dashed curve presents the unpolarized photon spectrum. The choice of polarizations improves the monochromatization and enhances the effective energy of the photon collider. Another important measure is the average polarization of the backscattered photon beam. Figure 1(b) illustrates the average percentage polarization for various choices of initial beam polarizations. The solid curve is the preferred choice in terms of the energy spectrum and it is also desirable that it yields almost purely right-handed polarized beam near the peak  $x \sim 0.8$ .

After integrating over the azimuthal angles, the differential cross section can be expressed as [20]

$$d\sigma(\hat{s})_{\gamma\gamma \rightarrow nV} = d\sigma_+ + \zeta_2 \tilde{\zeta}_2 d\sigma_-, \quad (15)$$

$$d\sigma_{\pm} = \frac{1}{4} (|M_{++}|^2 + |M_{--}|^2 \pm |M_{+-}|^2 \pm |M_{-+}|^2) dPS_n \quad (16)$$

where  $M_{\sigma_1\sigma_2}$  are the helicity amplitudes for two photons with helicity  $\sigma_1, \sigma_2$ , and  $dPS_n$  the  $n$ -body phase space element.  $\zeta_2$  and  $\tilde{\zeta}_2$  are the Stokes parameters [20] for the two colliding photon beams

$$\begin{aligned} \zeta_2 &= \frac{C_{20}}{C_{00}}, \quad r \equiv \frac{x}{\xi(1-x)}, \\ C_{00} &= \frac{1}{1-x} + 1 - x - 4r(1-r) - 2\lambda_e P_c r \xi (2r-1)(2-x) \\ C_{20} &= 2\lambda_e r \xi [1 + (1-x)(2r-1)^2] - P_c (2r-1) \left( \frac{1}{1-x} + 1 - x \right), \end{aligned}$$

and  $\tilde{\zeta}_2$  is of the same form for the other photon.

We are considering the anomalous gauge couplings with the existence of a light Higgs boson. For definitiveness, we will take its mass to be in the range

$$115 \text{ GeV} \leq m_H \leq 300 \text{ GeV}. \quad (17)$$

When searching for anomalous  $HVV$  couplings, we consider the signal as the excess or deficit from the SM prediction. The backgrounds are the SM expectation corresponding to  $f_n/\Lambda^2 = 0$ . We thus define the background cross section  $\sigma_B$  and the signal cross section  $\sigma_S$  by

$$\sigma_B \equiv \sigma(f_n/\Lambda^2 = 0), \quad \sigma_S \equiv \sigma(f_n/\Lambda^2 \neq 0) - \sigma_B. \quad (18)$$

With the corresponding background and signal event numbers  $N_B$  and  $N_S$ , the statistical significance  $\sigma_{stat}$  is defined by

$$\sigma_{stat} \equiv \frac{N_S}{\sqrt{N_S + N_B}}. \quad (19)$$

In the following numerical calculations, we take the integrated luminosity of an  $e^+e^-$  collider to be  $\int \mathcal{L} dt = 1 \text{ ab}^{-1}$ , which corresponds to about a two-year run at 0.5 TeV and 1 TeV for the International Linear Collider (ILC) roughly estimated from the TESLA Technical Design Report [22], and about a 1-year run at 3 TeV for the CERN Compact Linear Collider (CLIC) [23].

#### IV. SENSITIVITY TO THE ANOMALOUS COUPLINGS FROM $\gamma\gamma \rightarrow ZZ$

When considering gauge boson pair production at a photon collider to probe the EWSB beyond the SM, as pointed out in Ref. [24], the  $\gamma\gamma \rightarrow W^+W^-$  process suffers from a large tree-level SM background, while  $\gamma\gamma \rightarrow ZZ$  is free from tree-level SM backgrounds. We therefore concentrate on this process in this section.

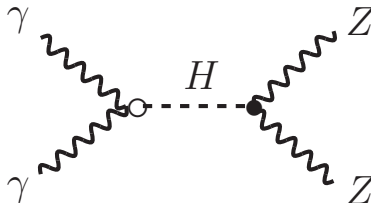


FIG. 2: Feynman diagram for the signal process  $\gamma\gamma \rightarrow ZZ$ . The vertex with a circle  $\circ$  stands for the anomalous  $H\gamma\gamma$  interaction with the anomalous coupling constant  $g_{H\gamma\gamma}$ , and the vertex with a black dot  $\bullet$  contains the SM coupling and the anomalous  $HZZ$  interactions with the anomalous couplings  $g_{HZZ}^{(1)}$  and  $g_{HZZ}^{(2)}$ .

With the anomalous  $H\gamma\gamma$  coupling, the signal process  $\gamma\gamma \rightarrow ZZ$  can formally have a tree level contribution shown in Fig. 2, in which the vertex with a circle contains only the anomalous  $H\gamma\gamma$  interaction with the coupling  $g_{H\gamma\gamma}$ , and the vertex with a black dot contains the SM interaction as well as the anomalous  $HZZ$  interactions with the anomalous coupling  $g_{HZZ}^{(1)}$  and  $g_{HZZ}^{(2)}$ . Our calculation shows that, for reasonable values of  $g_{HZZ}^{(1)}$  and  $g_{HZZ}^{(2)}$  and center of mass energy, the contribution of the anomalous  $HZZ$  interactions to the cross section is only a few percent relative to the SM contribution. Therefore the process  $\gamma\gamma \rightarrow ZZ$  mainly tests the anomalous couplings  $g_{H\gamma\gamma}$  which is related to  $(f_{BB} + f_{WW})/\Lambda^2$  [cf. Eq. (6)]. Studying  $W^+W^+$  scattering at the LHC on the other hand provides a sensitive test of  $f_W/\Lambda$  and/or  $f_{WW}/\Lambda$ , but it is not sensitive to  $f_B/\Lambda^2$  and  $f_{BB}/\Lambda^2$  [12]. The present process  $\gamma\gamma \rightarrow ZZ$  thus provides complementary information about  $f_{BB}/\Lambda^2$ . We note



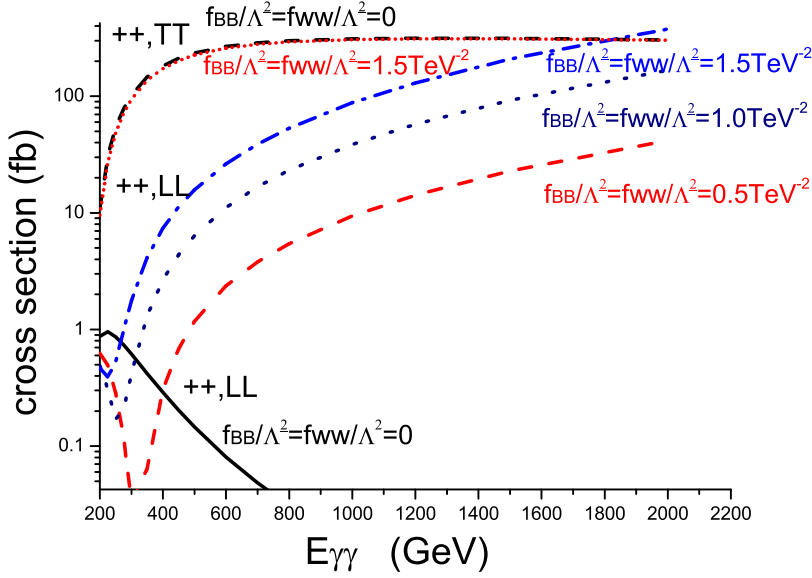


FIG. 3: Energy dependence of the signal and background cross sections for  $\gamma_+\gamma_+ \rightarrow Z_L Z_L$  and  $\gamma_+\gamma_+ \rightarrow Z_T Z_T$  in the case of  $m_H = 115$  GeV. The symbol  $+$  labels the photon helicity, and the symbols  $++$ ,  $LL$  and  $++$ ,  $TT$  stand for  $\gamma_+\gamma_+ \rightarrow Z_L Z_L$  and  $\gamma_+\gamma_+ \rightarrow Z_T Z_T$ , respectively. For simplicity, we take  $f_{BB}/\Lambda^2 = f_{WW}/\Lambda^2 \equiv f/\Lambda^2$ . The curves with  $f/\Lambda^2 = 0$  are the SM backgrounds.

that the signal process is via an  $s$ -channel scalar exchange, so that only the two photons with same helicities contribute, while the leading SM backgrounds come from one-loop box diagrams and thus are of all partial wave contributions [25]. In our background calculations, we take  $m_t = 174$  GeV.

#### A. The case of polarized photon colliders

As noted above, the like-sign helicities for the two photon beams are preferred by the signal. We thus first consider the case of polarized photon colliders. It is instructive to examine the final state  $Z$  bosons with specific polarizations and see the comparison for the signal and SM background expectation. We illustrate this by plotting the energy dependence of the cross sections with representative values of the anomalous couplings for various  $Z$  polarizations in FIG. 3. We label the photon circular polarizations by  $\pm\pm$ , and the longitudinal (transverse) polarizations of the final state  $Z$  bosons by  $LL$  ( $TT$ ). The  $\gamma_+\gamma_+ \rightarrow Z_L Z_L$  cross section  $\sigma(++LL)$  and the  $\gamma_+\gamma_+ \rightarrow Z_T Z_T$  cross sections  $\sigma(++TT)$  are shown as functions of the collision energy  $E_{\gamma\gamma}$  for  $m_H = 115$  GeV. The cross section for  $Z_L Z_T$  is so small that we have ignored it.

We first look at the SM cross sections for longitudinally and transversely polarized  $ZZ$  labeled by

$\sigma(++TT, f/\Lambda^2 = 0)$  and  $\sigma(++LL, f/\Lambda^2 = 0)$ , respectively. At high energies,  $\sigma(++TT, f/\Lambda^2 = 0)$  is dominantly from the  $W^\pm$ -loop diagrams [25] in which the vertices emitting the  $Z_T$  boson are momentum-dependent. So  $\sigma(++TT, f/\Lambda = 0)$  is large, and it does not fall off with  $E_{\gamma\gamma}$  in the energy range shown in FIG. 3. The situation of  $\sigma(++LL, f/\Lambda^2 = 0)$  is different. It is easier to understand it by invoking the equivalence theorem for Goldstone bosons and longitudinal weak bosons [26]. According to the equivalence theorem,  $Z_L$  can be treated as a would-be Goldstone boson  $z^0$ . The vertices emitting  $z^0$  in the  $W^\pm$ -loop diagrams and the  $H z^0 z^0$  vertex in the diagram with an  $s$ -channel Higgs boson are all momentum independent, and the  $H z^0 z^0$  coupling strength of  $\lambda \propto m_H^2/v^2$  ( $v=246$  GeV) is weak for a light Higgs with  $m_H$  smaller than  $v$ . So  $\sigma(++LL, f/\Lambda^2 = 0)$  is significantly smaller than  $\sigma(++TT, f/\Lambda^2 = 0)$  and it falls off rapidly with  $E_{\gamma\gamma}$  as is seen in the figure. This implies that the SM background is mainly  $\sigma(++TT, f/\Lambda^2 = 0)$ , especially in the energy region above 300 GeV.

Next we look at the cross sections with  $f/\Lambda^2 \neq 0$ . From FIG. 3 we see that  $\sigma(++TT, f/\Lambda^2 \neq 0)$  is very close to the SM cross section  $\sigma(++TT, f/\Lambda^2 = 0)$ . This means that the signal cross section  $\sigma_S(++TT) \equiv \sigma(++TT, f/\Lambda^2 \neq 0) - \sigma(++TT, f/\Lambda^2 = 0)$  defined in Eq. (18) is negligibly small. The signal of  $f/\Lambda^2 \neq 0$  is thus dominated by the  $++LL$  channel. Due to the momentum dependence of the longitudinal polarization vector, the anomalous coupling  $f/\Lambda^2 \neq 0$  causes extra energy-dependence of  $\sigma(++LL, f/\Lambda^2 \neq 0)$  [12]. We see that  $\sigma(++LL, f/\Lambda^2 \neq 0)$  increases rapidly with  $E_{\gamma\gamma}$  (below the new physics scale  $\Lambda$ ), and it becomes larger than the SM cross section  $\sigma(++LL, f/\Lambda^2 = 0)$  at high energies. Therefore the signal cross section  $\sigma_S(++LL) \equiv \sigma(++LL, f/\Lambda^2 \neq 0) - \sigma(++LL, f/\Lambda^2 = 0)$  is large and increases very rapidly with  $E_{\gamma\gamma}$ . We note from FIG. 3 that there is destructive interference between the SM amplitude and that of  $(++LL, f/\Lambda^2 \neq 0)$ . The interference would become constructive if we flip the sign of  $f_n$ . However, the effects are only at lower energies  $E_{\gamma\gamma} \leq 300$  GeV and are nevertheless rather small. The interference effects at high energies are essentially diminished. As seen in FIG. 3, the SM background of  $Z_L Z_L$  production falls off very rapidly at higher energies and the signal rate increases with respect to the anomalous couplings as  $(f/\Lambda^2)^2$ . One may wonder if we should include the dimension-8 operators as well which is of  $O(1/\Lambda^4)$  and is important at high energies. In fact, our approximation is well justified. For the dimension-8 operators, the linear terms proportional to  $1/\Lambda^4$  arise from the interference with the SM amplitude, which are much smaller for the reason stated above.

At higher energies, the signal cross section  $\sigma_S(++LL, f/\Lambda^2 \neq 0)$  may exceed the SM background  $\sigma(++TT, f/\Lambda^2 = 0)$ . However, in the energy region below 1.5 TeV, the signal  $\sigma_S(++LL, f/\Lambda^2 \neq 0)$  is still smaller than the background  $\sigma(++TT, f/\Lambda^2 = 0)$ . In addition to  $\sigma(++TT, f/\Lambda^2 = 0)$

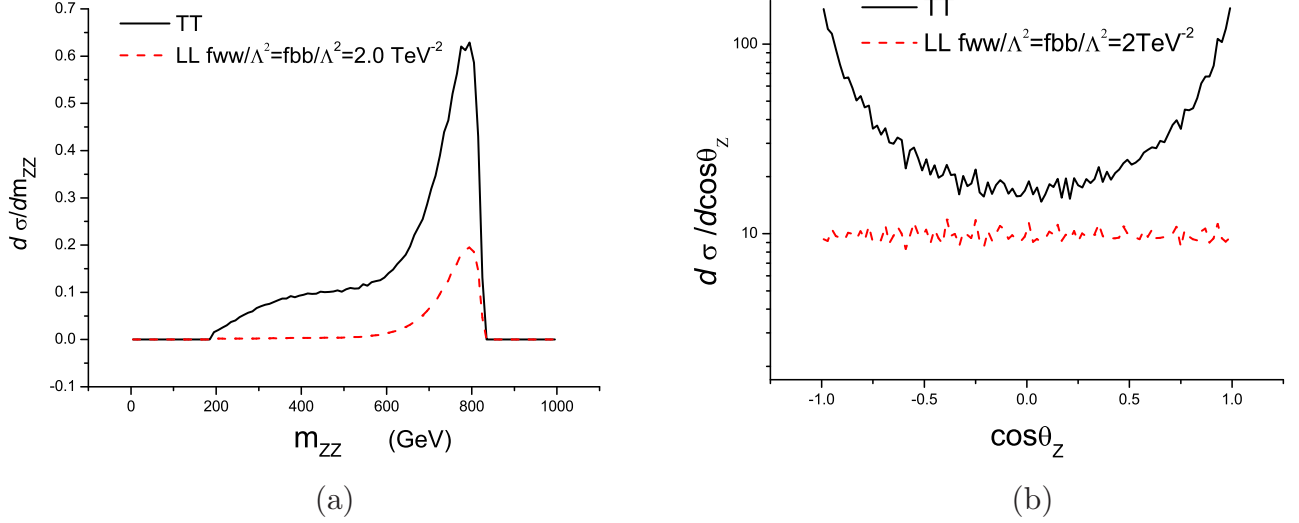


FIG. 4: Differential distributions for (a) the invariant mass  $M_{ZZ}$  and (b)  $\theta_Z$  at  $\sqrt{s_{ee}} = 1$  TeV in the  $e^+e^-$  collision system after imposing the cut (20). The solid curve is the SM background  $\sigma(TT, f/\Lambda^2 = 0)$  and the dashed curve is the signal  $\sigma(++LL, f/\Lambda^2 = 2.0 \text{ TeV}^{-2})$ .

considered above, there is also SM backgrounds  $\sigma(\pm\mp TT, f/\Lambda^2 = 0)$  from  $\gamma_\pm\gamma_\mp$  collisions, which are comparable to the  $\sigma(++TT, f/\Lambda^2 = 0)$  [25]. Over all, we see that the SM background is substantially larger than the signal except at very high energies. Thus we need to develop suitable kinematic cuts to suppress the SM backgrounds, as we discuss next.

Our first cut is for suppressing the  $\gamma_+\gamma_-$  contribution. We know that the colliding photon energy will peak around 80% of the  $e^+e^-$  colliding energy with a tail in the low energy region if we take the polarization satisfying  $2\lambda_e P_c = -1$  [cf. FIG. 1(a)] [20]. The corresponding  $\omega/E_e$  distribution of the mean helicity  $\lambda_r$  of the colliding photon for various polarizations has been given in Ref. [21] which is shown in Fig. 1(b). We see from curve *a* in Fig. 1(b) ( $2\lambda_e P_c = -1$ ) that the mean helicity is nearly  $\lambda_r \approx +1$  in the region  $0.65 < \omega/E_e < 0.8$ . Therefore we can envision to impose this condition to strongly suppressed the background. In FIG. 4(a), we plot the  $M_{ZZ}$  distribution for the signal  $\sigma(++LL, f/\Lambda^2 = 2 \text{ TeV}^{-2})$  and the background  $\sigma(TT, f/\Lambda^2 = 0)$  at  $\sqrt{s_{ee}} = 1$  TeV. This motivates us to introduce a cut on the invariant mass of the final state  $ZZ$

$$M_{ZZ} > 0.65\sqrt{s_{ee}}. \quad (20)$$

Numerically, we find that the cut (20) reduces the background  $\sigma(TT, f/\Lambda^2 = 0)$  from 115 fb to 72 fb down by 37%, but the signal  $\sigma(++LL, f/\Lambda^2 = 2 \text{ TeV}^{-2})$  only from 22 fb to 20 fb. After imposing the cut in (20), the SM background contains mainly  $\sigma(++TT, f/\Lambda^2 = 0)$  shown in FIG. 3.

Our second cut concerns the angular distribution of the final state  $Z$  bosons. In FIG. 4(b), we plot

the  $\theta_Z$  distributions of the signal  $\sigma(++LL, f/\Lambda^2 = 2 \text{ TeV}^{-2})$  and the background  $\sigma(++TT, f/\Lambda^2 = 0)$  at a  $\sqrt{s_{ee}} = 1 \text{ TeV}$  linear collider, where  $\theta_Z$  is the polar angle of the final state  $Z$  boson with respect to the colliding beam  $e^-$  axis in the center of mass frame of  $ZZ$ . As expected,  $d\sigma(LL, f/\Lambda^2 = 2 \text{ TeV}^{-2})/d\cos\theta_Z$  is isotropic, while  $d\sigma(TT, f/\Lambda^2 = 0)/d\cos\theta_Z$  is strongly forward and backward. Therefore we impose

$$-0.5 < \cos\theta_Z < 0.5. \quad (21)$$

We find that, after this cut,  $\sigma(TT, f/\Lambda^2 = 0)$  is reduced from 72 fb to 16 fb, while  $\sigma(LL, f/\Lambda^2 = 2 \text{ TeV}^{-2})$  changes from 20 fb to 9 fb.

It is known that the angular distribution for a fermion from  $Z$  decay goes like

$$\frac{d\sigma}{d\cos\theta_f} \propto \begin{cases} 1 + \cos^2\theta_f & \text{for } Z_T, \\ \sin^2\theta_f & \text{for } Z_L, \end{cases}$$

where  $\theta_f$  is the polar angle for a final state fermion  $f$  in the rest frame of  $Z$  with respect to the  $Z$  momentum direction in the center of mass frame of  $ZZ$ . We thus propose a third cut

$$|\cos\theta_f| < 0.5. \quad (22)$$

In the example of  $\sqrt{s_{ee}} = 1 \text{ TeV}$ , this cut reduces the background cross section from 16 fb to 3.5 fb, while it reduces  $\sigma(LL, f/\Lambda^2 = 2 \text{ TeV}^{-2})$  from 9 fb to 5 fb. To measure the effectiveness of our cuts, we define a double-ratio

$$r \equiv \frac{\sigma_{LL}(\text{after cut})/\sigma_{LL}(\text{before cut})}{\sigma_{TT}(\text{after cut})/\sigma_{TT}(\text{before cut})}. \quad (23)$$

The larger the value of this ratio is, the more effective the cuts are in terms of the signal enhancement over the background suppression. The effects of the three cuts are summarized in TABLE II for  $\sqrt{s_{ee}} = 1$  and 3 TeV.

Next we consider the actual detection of the final state  $Z$  bosons via the decay products. We only consider the fully reconstructable modes  $Z \rightarrow \ell^+\ell^-$  ( $\ell = e, \mu$ ) and  $jj$ , with branching ratios [1]

$$B(Z \rightarrow e^+e^-) = B(Z \rightarrow \mu^+\mu^-) \approx 3.36\%, \quad B(Z \rightarrow jj) \approx 70\%.$$

For the two final state  $Z$  bosons, we can have the pure leptonic modes  $ZZ \rightarrow \ell^+\ell^- \ell^+\ell^-$ , semi-leptonic modes  $ZZ \rightarrow \ell^+\ell^- jj$ , and the hadronic modes  $ZZ \rightarrow jj jj$ . We require the reconstruction of  $Z$  bosons by the invariant mass of the decay products  $M_Z \approx M(\ell^+\ell^-)$ ,  $M(jj)$ . For the hadronic mode, some care needs to be taken due to the potentially large background  $\gamma\gamma \rightarrow W^+W^- \rightarrow jjjj$ . It has been

TABLE II: The cut effectiveness  $r$  as defined in Eq. (23), in terms of the effects of the cuts (20), (21), and (22) in the case of the  $\sqrt{s_{ee}} = 1$  TeV ILC with  $f/\Lambda^2 = 2 \text{ TeV}^{-2}$  and the case of the  $\sqrt{s_{ee}} = 3$  TeV CLIC with  $f/\Lambda^2 = 1 \text{ TeV}^{-2}$ . The symbols  $\sigma_{LL}$  and  $\sigma_{TT}$  stand for  $\sigma(++LL, f/\Lambda^2 \neq 0)$  and the background cross section, respectively.

		no cuts	cut (20)	cuts (20)+(21)	cuts (20)+(21)+(22)
$\sqrt{s_{ee}} = 1 \text{ TeV}$	$\sigma_{LL} \text{ (fb)}$	22	20	9.2	4.9
	$\sigma_{TT} \text{ (fb)}$	115	72	16	3.5
	$r$	—	90%/63% $\approx 1.4$	47%/22% $\approx 2.1$	54%/22% $\approx 2.5$
$\sqrt{s_{ee}} = 3 \text{ TeV}$	$\sigma_{LL} \text{ (fb)}$	58	51	24	12.2
	$\sigma_{TT} \text{ (fb)}$	190	85	6.5	1.1
	$r$	—	88%/45% $\approx 2.0$	47%/7.6% $\approx 6.2$	51%/17% $\approx 3.0$

emphasized that it is important for the detector to be able to distinguish the hadronic decays of the  $Z$  and  $W$  from their mass reconstruction [27]. As a conservative estimate for the reconstruction efficiency, we include another factor 50% for the  $ZZ$  hadronic modes. Then the total detection efficiency for the final state  $ZZ$  under consideration is

$$\epsilon = (3.36\% + 3.36\%)^2 + 2 \times (3.36\% + 3.36\%) \times 70\% + (70\%)^2 \times 50\% \approx 34\%. \quad (24)$$

For comparison with the LHC results of Ref. [12], we make the same assumption  $f_{BB}/\Lambda^2 = f_{WW}/\Lambda^2 \equiv f/\Lambda^2$  for illustration. The event rates can be calculated using Eqs. (15) and (24). Assuming an integrated luminosity of  $1 \text{ ab}^{-1}$ , we obtain the number of events in FIG. 5(a) for  $m_H = 115, 200$  and  $300 \text{ GeV}$  at a  $\sqrt{s_{ee}} = 500 \text{ GeV}$  polarized ILC with the cuts (20), (21) and (22). The symbols of the bullet, square, triangle and asterisk on each curve mark the values corresponding to  $1\sigma, 2\sigma, 3\sigma$  and  $5\sigma$  statistical significance  $\sigma_{stat}$  of Eq. (19), respectively. The numbers of events are above 1300 for  $m_H = 115 - 300 \text{ GeV}$ . It is not so sensitive to  $m_H$ , but varies quite sensitively with respect to the value of  $f/\Lambda^2$ .

At this kind of energy, in the case of  $m_H = 115 - 200 \text{ GeV}$ , the signal cross section is comparable to that of the SM background after the cuts. There is considerable interference between the two amplitudes, which causes the numbers of events asymmetric near  $f/\Lambda^2 \approx 0$ . If no  $f/\Lambda^2 \neq 0$  signal effect is observed at the ILC, it would lead to sensitive bounds on the anomalous couplings. From FIG. 5(a) for  $m_H = 115 - 200 \text{ GeV}$ , we obtain the  $2\sigma$  and  $3\sigma$  bounds for  $f/\Lambda^2$  and  $g_{H\gamma\gamma}$  [cf. Eq. (6)]:

$$\sqrt{s_{ee}} = 500 \text{ GeV polarized ILC, } m_H = 115 - 200 \text{ GeV} :$$

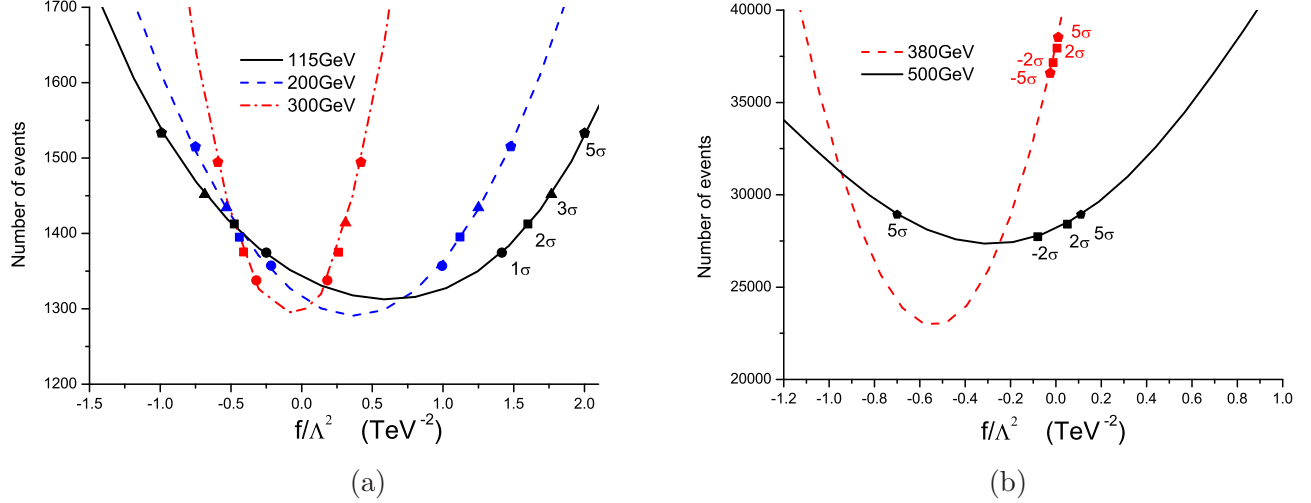


FIG. 5: Numbers of events of  $\gamma\gamma \rightarrow ZZ$  ( $Z \rightarrow e^+e^-, \mu^+\mu^-, jj$ ) versus  $f/\Lambda^2$ : (a) for  $m_H = 115$  GeV, 200 GeV and 300 GeV at a  $\sqrt{s_{ee}} = 500$  GeV polarized ILC with the cuts (20), (21) and (22) imposed, (b) for  $m_H = 300$  GeV at a  $\sqrt{s_{ee}} = 500$  GeV polarized ILC (solid curve) and a  $\sqrt{s_{ee}} = 380$  GeV polarized ILC (dashed curve) without imposing the cuts (20), (21) and (22). The values of  $f/\Lambda^2$  corresponding to  $1\sigma$ ,  $2\sigma$ ,  $3\sigma$  and  $5\sigma$  statistical deviations [cf. Eq. (19)] are shown on each curve by the  $f/\Lambda^2$ -coordinates of the bullet, square, triangle and asterisk, respectively.

$$\begin{aligned}
2\sigma: \quad & -0.48 \text{ TeV}^{-2} < f/\Lambda^2 < 1.6 \text{ TeV}^{-2}, \quad -0.019 \text{ TeV}^{-1} < g_{H\gamma\gamma} < 0.0058 \text{ TeV}^{-1}, \\
3\sigma: \quad & -0.68 \text{ TeV}^{-2} < f/\Lambda^2 < 1.8 \text{ TeV}^{-2}, \quad -0.022 \text{ TeV}^{-1} < g_{H\gamma\gamma} < 0.0082 \text{ TeV}^{-1}. \quad (25)
\end{aligned}$$

This  $2\sigma$  constraint on  $g_{H\gamma\gamma}$  is comparable to those in the literature [13] from the other processes. From the results in Ref. [12] we can see that the  $2\sigma$  ( $3\sigma$ ) constraints on  $f_{WW}/\Lambda^2$  and  $g_{H\gamma\gamma}$  obtained from  $W^+W^+$  scattering at the LHC are

$$|f_{WW}/\Lambda^2| \leq 2.2 \text{ TeV}^{-2} \quad (3.0 \text{ TeV}^{-2}), \quad |g_{H\gamma\gamma}| < 0.027 \text{ TeV}^{-1} \quad (0.036 \text{ TeV}^{-1}). \quad (26)$$

Comparing with our results in Eq. (25) for  $\gamma\gamma \rightarrow ZZ$ , we see that the upper bound would be improved over the LHC results by a factor about 1.5, and the lower bound by roughly a factor of 4.

The case of  $m_H = 300$  GeV at the 500 GeV ILC is rather special. Even with the cut (20), the tail of the resonance still enhances the contribution in the  $s$ -channel Higgs diagrams (e.g. FIG. 2). On the other hand, the SM background via the  $s$ -channel Higgs boson exchange does not increase as much. Consequently, the number of events for  $f/\Lambda^2 \neq 0$  is significantly larger for  $m_H = 300$  GeV than those for  $m_H = 115 - 200$  GeV. Thus the test for  $m_H = 300$  GeV is much more sensitive than that for  $m_H = 115 - 200$  GeV. Because the resonance enhancement is more significant in the signal amplitude of FIG. 2 than in the SM amplitude, we may even consider relaxing the cuts (20), (21), and (22). Although the SM background is less suppressed without imposing the cuts, the signal to background

ratio can still be improved. For illustration, the result for  $m_H = 300$  GeV without those cuts is plotted as the solid curve in FIG. 5(b). When including the resonant signal, the number of events can be increased by an order of magnitude. The sensitivity is much improved. The  $5\sigma$  sensitivity can constrain the couplings in the range

$$\begin{aligned} \sqrt{s_{ee}} &= 500 \text{ GeV polarized ILC (no cuts), } m_H = 300 \text{ GeV :} \\ 5\sigma : \quad &-0.7 \text{ TeV}^{-2} < f/\Lambda^2 < 0.11 \text{ TeV}^{-2}, \quad -0.0013 \text{ TeV}^{-1} < g_{H\gamma\gamma} < 0.0085 \text{ TeV}^{-1}. \end{aligned} \quad (27)$$

In practice, if a light Higgs boson with certain  $m_H$  is found at the LHC, we may consider tuning the colliding photon energy  $E_{\gamma\gamma}$  to be at the resonance value of the mass since the energy in the first phase of the ILC can be tuned between 200 GeV and 500 GeV. Then the event rate for the  $f/\Lambda^2 \neq 0$  amplitude shown in FIG. 2 is maximally enhanced, and we can reach the optimal sensitivity. This works for the cases with  $m_H > 2M_Z$ . Take the case of  $m_H = 300$  GeV as an example again. One can tune the ILC energy to be  $\sqrt{s_{ee}} = 380$  GeV so that the peak of  $E_{\gamma\gamma}$  is at 300 GeV. The calculated result in this case is plotted as the dashed curve in FIG. 5(b). The  $5\sigma$  sensitivity range is

$$\begin{aligned} \sqrt{s_{ee}} &= 380 \text{ GeV polarized ILC (without cuts), } m_H = 300 \text{ GeV :} \\ 5\sigma : \quad &-0.025 \text{ TeV}^{-2} < f/\Lambda^2 < 0.010 \text{ TeV}^{-2}, \quad -0.00012 \text{ TeV}^{-1} < g_{H\gamma\gamma} < 0.00030 \text{ TeV}^{-1}. \end{aligned} \quad (28)$$

We see that the sensitivity can be very high. To put it into perspective, if  $f$  is naturally the order of unity, then the physical scale probed can be as high as  $\Lambda \sim 10$  TeV. Note that we have only taken into account the statistical error here. With the systematic error (depending on the property of the detectors), the actual sensitivity may be accordingly lower.

Next we consider the cases of  $\sqrt{s_{ee}} = 1$  TeV polarized ILC and  $\sqrt{s_{ee}} = 3$  TeV polarized CLIC for  $m_H = 115 - 300$  GeV. The obtained results are plotted in FIG. 6. We see that the SM backgrounds are almost independent of  $m_H$  as the values shown at  $f/\Lambda^2 = 0$ . Furthermore, for  $\sqrt{s_{ee}} = 3$  TeV in FIG. 6(b), the event rates are essentially symmetric near  $f/\Lambda^2 = 0$ , due to the large signal rate and small interference with the SM amplitude. In the absence of a signal observation, FIG. 6(a) and (b) lead to the following  $2\sigma$  and  $3\sigma$  statistical bounds

$$\begin{aligned} \sqrt{s_{ee}} &= 1 \text{ TeV polarized ILC (with cuts), } m_H = 115 - 300 \text{ GeV :} \\ 2\sigma : \quad &-0.32 \text{ TeV}^{-2} < f/\Lambda^2 < 0.50 \text{ TeV}^{-2}, \quad -0.0061 \text{ TeV}^{-1} < g_{H\gamma\gamma} < 0.0048 \text{ TeV}^{-1}, \\ 3\sigma : \quad &-0.40 \text{ TeV}^{-2} < f/\Lambda^2 < 0.60 \text{ TeV}^{-2}, \quad -0.0073 \text{ TeV}^{-1} < g_{H\gamma\gamma} < 0.0054 \text{ TeV}^{-1}. \end{aligned} \quad (29)$$

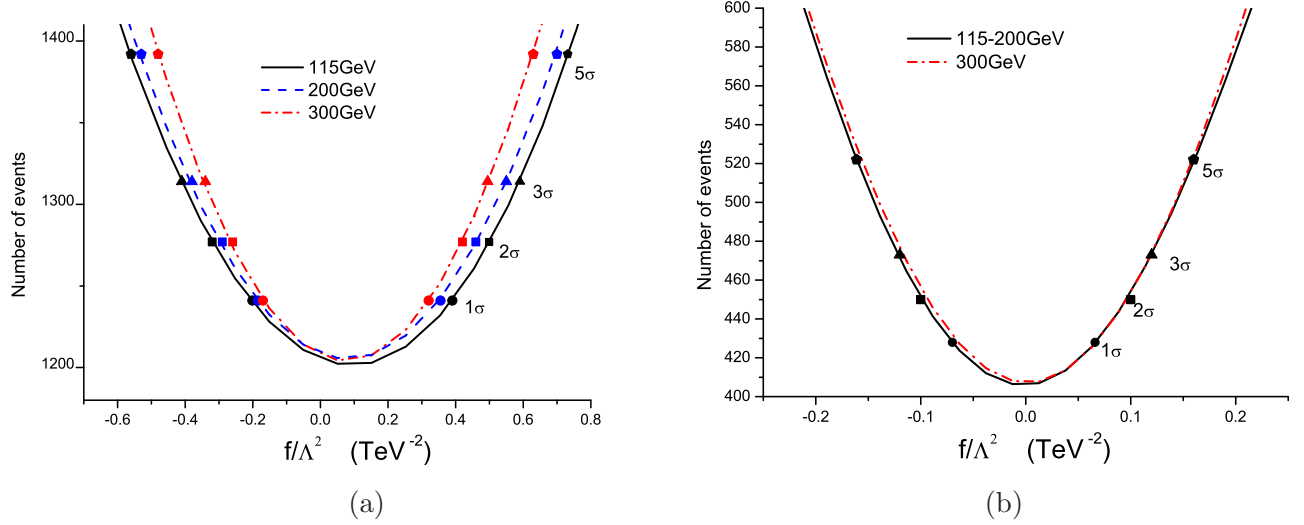


FIG. 6: Numbers of events of  $\gamma\gamma \rightarrow ZZ$  ( $Z \rightarrow e^+e^-, \mu^+\mu^-, jj$ ) versus  $f/\Lambda^2$  for  $m_H = 115$  GeV, 200 GeV and 300 GeV with the cuts (20), (21) and (22): (a) at a  $\sqrt{s_{ee}} = 1$  TeV polarized ILC, (b) at a  $\sqrt{s_{ee}} = 3$  TeV polarized CLIC. The values of  $f/\Lambda^2$  corresponding to  $1\sigma$ ,  $2\sigma$ ,  $3\sigma$  and  $5\sigma$  statistical deviations [cf. Eq. (19)] are shown on each curve by the  $f/\Lambda^2$ -coordinates of the bullet, square, triangle and asterisk, respectively.

$\sqrt{s_{ee}} = 3$  TeV polarized CLIC (with cuts),  $m_H = 115 - 300$  GeV :

$$\begin{aligned}
 2\sigma : \quad & -0.10 \text{ TeV}^{-2} < f/\Lambda^2 < 0.10 \text{ TeV}^{-2}, \quad -0.0012 \text{ TeV}^{-1} < g_{H\gamma\gamma} < 0.0012 \text{ TeV}^{-1}, \\
 3\sigma : \quad & -0.12 \text{ TeV}^{-2} < f/\Lambda^2 < 0.12 \text{ TeV}^{-2}, \quad -0.0015 \text{ TeV}^{-1} < g_{H\gamma\gamma} < 0.0015 \text{ TeV}^{-1}.
 \end{aligned} \tag{30}$$

We see that the present tests lead to very high sensitivities. The constraints on  $g_{H\gamma\gamma}$  are all of the order of  $10^{-3} \text{ TeV}^{-1}$ . Compared with the  $3\sigma$  constraints  $|f_{WW}/\Lambda^2| \leq 2.9 \text{ TeV}^{-2}$  and  $|g_{H\gamma\gamma}| < 0.036 \text{ TeV}^{-1}$  obtained from the results of  $W^+W^+$  scattering at the LHC in Ref. [12], the present sensitivities at  $\sqrt{s_{ee}} = 1$  TeV and  $\sqrt{s_{ee}} = 3$  TeV are improved by roughly a factor of 5 and 24, respectively.

### B. The case of unpolarized photon colliders

The production cross section at the unpolarized photon colliders can be calculated with Eq. (8). In the unpolarized case, the colliding photon energy distribution  $E_{\gamma\gamma}$  is less sharply peaked as seen in FIG. 1(a). This reduces the sensitivity with respect to the polarized case. The calculated results for  $m_H = 115, 130, 200, 300$  GeV at the  $\sqrt{s_{ee}} = 500$  GeV ILC, the 1 TeV ILC, and the 3 TeV CLIC with the same cuts (20), (21) and (22) are plotted in FIG. 7.

From FIG. 7(a) we see that the  $m_H = 300$  GeV case is again especially sensitive due to the nearly on-shell resonance effect as discussed earlier. For a lighter mass of  $m_H = 115$  and 200 GeV, the  $2\sigma$



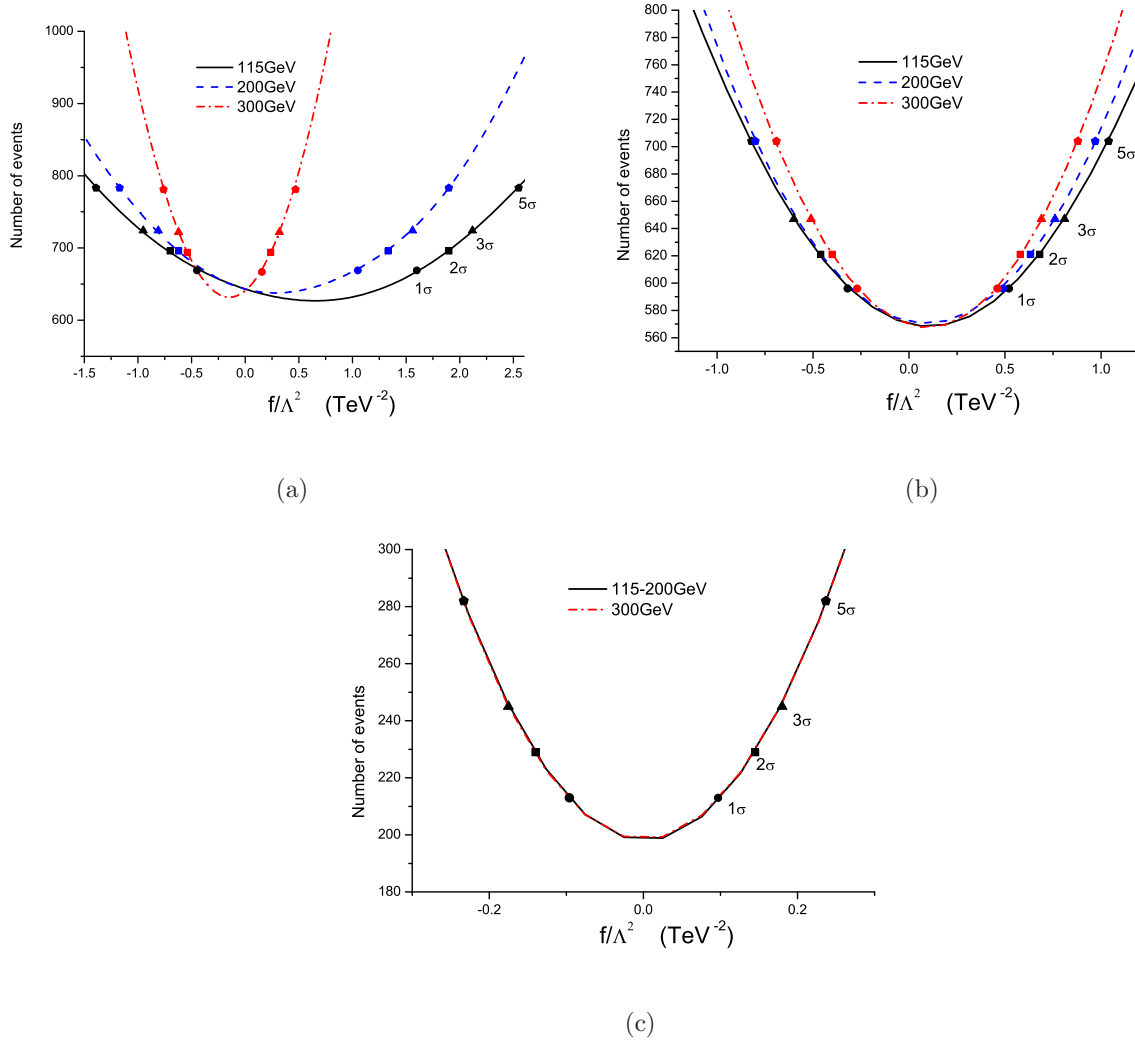


FIG. 7: Numbers of events of  $\gamma\gamma \rightarrow ZZ$  ( $Z \rightarrow e^+e^-, \mu^+\mu^-, jj$ ) versus  $f/\Lambda^2$  for  $m_H = 115$  GeV, 200 GeV and 300 GeV with the cuts (20), (21) and (22) at unpolarized linear colliders: (a) at a  $\sqrt{s_{ee}} = 500$  GeV ILC, (b) at a  $\sqrt{s_{ee}} = 1$  TeV ILC, and (c) at a  $\sqrt{s_{ee}} = 3$  TeV CLIC. The values of  $f/\Lambda^2$  corresponding to  $1\sigma$ ,  $2\sigma$ ,  $3\sigma$  and  $5\sigma$  statistical deviations [cf. Eq. (19)] are shown on each curve by the  $f/\Lambda^2$ -coordinates of the bullet, square, triangle and asterisk, respectively.

and  $3\sigma$  sensitivity bounds at the 500 GeV unpolarized ILC are

$$\begin{aligned}
 &\sqrt{s_{ee}} = 500 \text{ GeV unpolarized ILC (with cuts), } m_H = 115 - 200 \text{ GeV :} \\
 &2\sigma : \quad -0.7 \text{ TeV}^{-2} < f/\Lambda^2 < 1.9 \text{ TeV}^{-2}, \quad -0.023 \text{ TeV}^{-1} < g_{H\gamma\gamma} < 0.0085 \text{ TeV}^{-1}, \\
 &3\sigma : \quad -1.0 \text{ TeV}^{-2} < f/\Lambda^2 < 2.1 \text{ TeV}^{-2}, \quad -0.025 \text{ TeV}^{-2} < g_{H\gamma\gamma} < 0.012 \text{ TeV}^{-2}.
 \end{aligned} \tag{31}$$

These sensitivities are lower than those in Eq. (25) in the polarized case by roughly a factor of 1.2.

From FIG. 7(b) we see that the  $2\sigma$  and  $3\sigma$  testing sensitivities at the 1 TeV unpolarized ILC are

$$\sqrt{s_{ee}} = 1 \text{ TeV unpolarized ILC (with cuts), } m_H = 115 - 300 \text{ GeV :}$$

$$\begin{aligned}
2\sigma : \quad & -0.46 \text{ TeV}^{-2} < f/\Lambda^2 < 0.68 \text{ TeV}^{-2}, \quad -0.0082 \text{ TeV}^{-1} < g_{H\gamma\gamma} < 0.0056 \text{ TeV}^{-1}, \\
3\sigma : \quad & -0.60 \text{ TeV}^{-2} < f/\Lambda^2 < 0.81 \text{ TeV}^{-2}, \quad -0.0098 \text{ TeV}^{-2} < g_{H\gamma\gamma} < 0.0073 \text{ TeV}^{-2}.
\end{aligned} \tag{32}$$

These are lower than that in the polarized case [cf. Eq. (29)] by roughly a factor of 1.3.

From FIG. 7(c) we see that the  $2\sigma$  and  $3\sigma$  testing sensitivity at the 3 TeV unpolarized CLIC are

$$\begin{aligned}
& \sqrt{s_{ee}} = 3 \text{ TeV unpolarized CLIC (with cuts), } m_H = 115 - 300 \text{ GeV :} \\
2\sigma : \quad & -0.14 \text{ TeV}^{-2} < f/\Lambda^2 < 0.14 \text{ TeV}^{-2}, \quad -0.0017 \text{ TeV}^{-1} < g_{H\gamma\gamma} < 0.0017 \text{ TeV}^{-1}, \\
3\sigma : \quad & -0.18 \text{ TeV}^{-2} < f/\Lambda^2 < 0.18 \text{ TeV}^{-2}, \quad -0.0022 \text{ TeV}^{-1} < g_{H\gamma\gamma} < 0.0022 \text{ TeV}^{-1}.
\end{aligned} \tag{33}$$

These are lower than that in the polarized case [cf. Eq. (30)] by roughly a factor of 1.4.

We conclude that suitable polarization of the photon collider does increase the testing sensitivities relative to the unpolarized case by roughly a factor of 1.2 – 1.4.

## V. SENSITIVITY TO THE ANOMALOUS COUPLINGS FROM $\gamma\gamma \rightarrow WWWW$

In order to avoid the large SM background in  $\gamma\gamma \rightarrow W_T W_T, Z_T Z_T$ , it was suggested in Refs. [28, 29] to make use of the processes  $\gamma\gamma \rightarrow WWWW$  and  $\gamma\gamma \rightarrow WWZZ$  to study strongly interacting EWSBM without a light Higgs boson. The signals and backgrounds in these processes were carefully studied in Ref. [30]. Here we explore the anomalous gauge couplings of the light Higgs boson [cf. Eqs. (1)–(6)] by the process

$$\gamma\gamma \rightarrow WWWW. \tag{34}$$

It is easy to show that the  $\gamma\gamma \rightarrow WWWW$  process is mainly sensitive to the anomalous coupling  $f_{WW}/\Lambda^2$  and  $f_W/\Lambda^2$  but not to  $f_B/\Lambda^2$  and  $f_{BB}/\Lambda^2$ . This is because that  $f_B/\Lambda^2$  and  $f_{BB}/\Lambda^2$  appear in  $g_{HVV}^{(i)}$ 's with coefficients proportional to power(s) of  $\sin \theta_W$  [cf. Eq. (6)]. In the following, we study  $f_{WW}/\Lambda^2$  and  $f_W/\Lambda^2$  assuming only one dominant at a time.

The Feynman diagrams for the process of Eq. (34) are shown in FIG. 8, in which the compact  $WWWW$  vertex collectively stands for the diagrams shown in FIG. 9, and the compact  $\gamma\gamma WW$  vertex stands for the diagrams shown in FIG. 10. FIG. 8(a)–8(d) indicate the contributions of the anomalous couplings  $f_{WW}/\Lambda^2$  and  $f_W/\Lambda^2$  to  $\gamma\gamma \rightarrow WWWW$  through its related anomalous  $HWW$ ,  $HZZ$ ,  $HZ\gamma$  and  $H\gamma\gamma$  interactions [cf. Eqs. (1)–(6)]. Note that the anomalous coupling  $g_{H\gamma\gamma}$  is related to  $s^2(f_{BB} + f_{WW})/\Lambda^2$  [cf. Eq. (6)]. Thus for the cases of  $f_{WW}/\Lambda^2$  or  $f_W/\Lambda^2$  dominance, FIG. 8(c) gives significant contribution only when  $f_{WW}/\Lambda^2$  is not too small. In the case of  $f_W/\Lambda^2$

dominance, i.e.,  $f_{WW}/\Lambda^2$ ,  $f_{BB}/\Lambda^2 \ll f_W/\Lambda^2$ , the contribution of FIG. 8(c) is negligibly small. We note that the cases of  $f_{WW}/\Lambda^2$  dominance or  $f_W/\Lambda^2$  dominance are quite different. The anomalous coupling  $f_{WW}/\Lambda^2$  ( $f_W/\Lambda^2$ ) also gives rise to the more complicated anomalous  $H\gamma WW$  and  $H\gamma\gamma WW$  interactions from the nonlinear gauge-field terms in  $\hat{W}_{\mu\nu}$  in  $\mathcal{O}_{WW}$  [cf. Eq. (4)]. These contributions are shown in FIG. 8(e) and 8(f). Since these terms contain higher powers of the weak interaction coupling constant  $g$ , their contributions are much smaller than those from FIG. 8(a)–8(d).

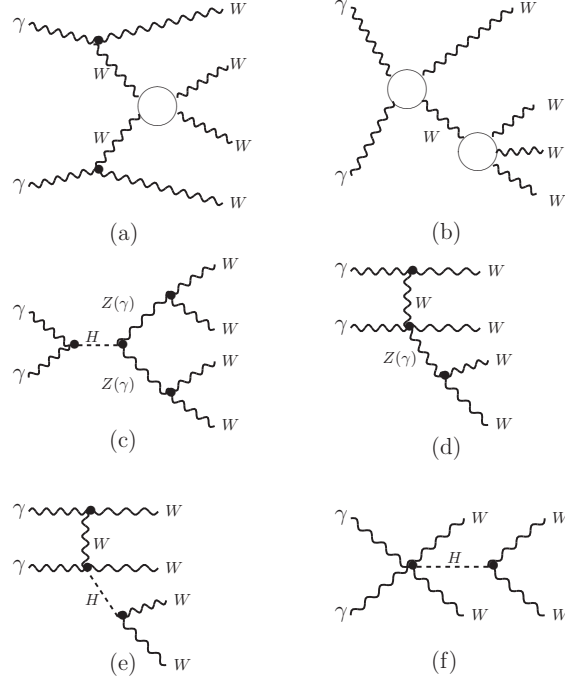


FIG. 8: Feynman diagrams for the process  $\gamma\gamma \rightarrow WWWW$ .

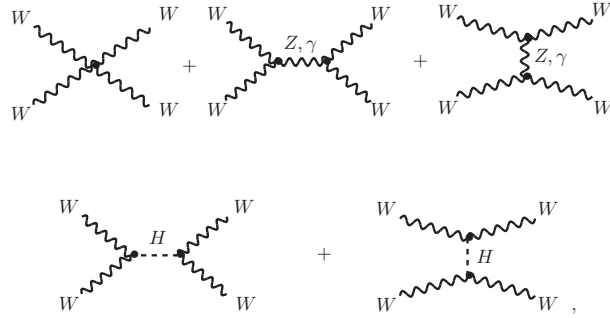


FIG. 9: Feynman diagrams in the  $WWWW$  vertex.

For the detection of the four final state  $W$  bosons, we take the hadronic decay mode  $W \rightarrow jj$ . Let  $\theta$  be the angle between two jets. Experimentally, the two jets can be resolved when  $\cos \theta < 0.8$  [31]. At high energy linear colliders, the  $W$  momenta are higher and consequently the two jets from the

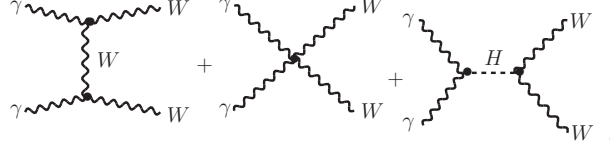


FIG. 10: Feynman diagrams in the  $AAWW$  vertex.

decay of a  $W$  boson are collimated along the  $W$  moving direction, so that the condition  $\cos \theta < 0.8$  can hardly be satisfied. However, we can still reconstruct the  $W$  boson by all the hadronic decay products in this wide jet to form a correct mass  $M_W$ . For distinguishing two of the final state  $W$  bosons, we require the isolation between any two jets from the  $i$ -th and  $j$ -th  $W$ -boson decays to satisfy

$$|\cos \theta_{ij}| < 0.8. \quad (35)$$

Here we approximately take the quarks from the  $W$  decays as the jets without performing hadronization and detector simulation. It turns out that the requirement (35) slightly improve the signal to background ratio. When estimating the detection efficiency, we take again a safety factor 50% for distinguishing the final state  $W$  bosons from  $Z$  bosons. We also take the integrated luminosity of  $1 \text{ ab}^{-1}$  to estimate the numbers of events.

We first note that for the  $\sqrt{s_{ee}} = 500 \text{ GeV}$  ILC, the effective colliding photon energy is typically less than  $400 \text{ GeV}$ , so that the  $\gamma\gamma \rightarrow WWWW$  process experiences severe phase space suppression and yields only a few events with  $1 \text{ ab}^{-1}$  luminosity. We will not pursue this case further. As for the case of the  $\sqrt{s_{ee}} = 1 \text{ TeV}$  ILC, with the requirement of Eq. (35), our calculation shows that there can be about 200–300 hundred events, and the  $2\sigma$  sensitivity for  $m_H = 115 \text{ GeV}$  is about  $-4.5 \text{ TeV}^{-2} < f_W/\Lambda^2 < 4.5 \text{ TeV}^{-2}$  and  $-20 \text{ TeV}^{-2} < f_{WW}/\Lambda^2 < 10 \text{ TeV}^{-2}$ . These are still weaker than those obtained from  $W^+W^+$  scattering at the LHC [12] as given in Eq. (7). Therefore,  $\gamma\gamma \rightarrow WWWW$  does not lead to an interesting process for testing the anomalous gauge couplings of the Higgs boson at the  $1 \text{ TeV}$  ILC.

Obviously, one would like to consider a higher energy reach for a more favorable kinematics for the  $4W$  production. This leads us to look at the case of the  $3 \text{ TeV}$  CLIC. Unlike the cases of the  $500 \text{ GeV}$  and  $1 \text{ TeV}$  ILC, for the case of  $f_{WW}/\Lambda^2$  dominance it is possible to impose certain kinematic cuts to further improve the signal to background ratio effectively at this energy. To see this, we divide the four final state  $W$  bosons into two groups according to their transverse momenta  $P_T$ . We denote the two  $W$  bosons with higher  $P_T$  by  $W_{h1}$  and  $W_{h2}$  with  $P_T(W_{h1}) < P_T(W_{h2})$ , for example the two scattered  $W$  bosons in the central rapidity region as in FIG. 8(a), and denote those two with lower  $P_T$  by  $W_{l1}$  and  $W_{l2}$  with  $P_T(W_{l1}) < P_T(W_{l2})$ , for example the two spectator  $W$  bosons in FIG. 8(a).

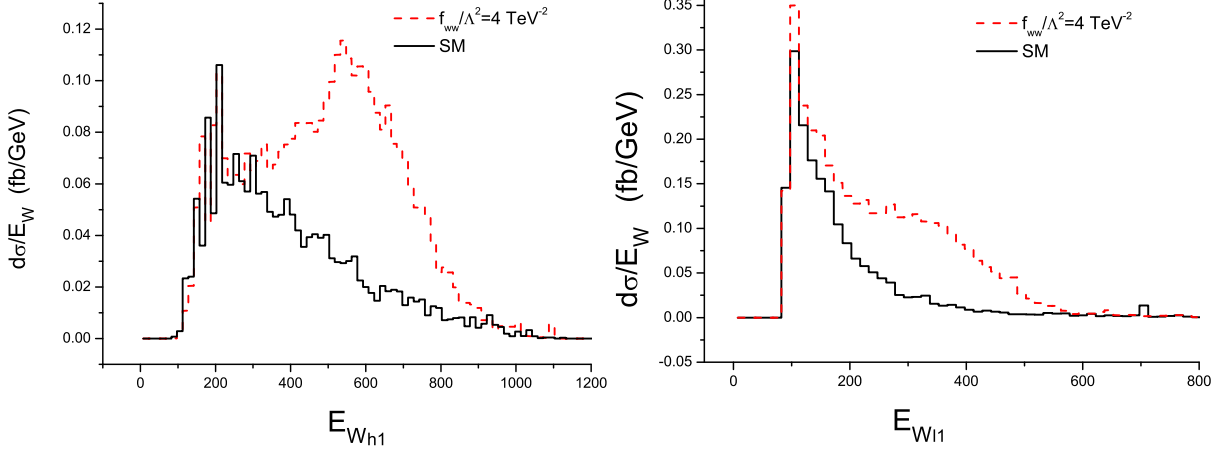


FIG. 11: Energy distributions for  $E_{W_{h1}}$  and  $E_{W_{l1}}$  with  $f_{WW}/\Lambda^2 = 4 \text{ TeV}^{-2}$  and  $f_{WW}/\Lambda^2 = 0$  (SM).

We first study the energy distributions  $E_{W_{h1}}$  and  $E_{W_{l1}}$  for  $f_{WW}/\Lambda^2 = 0$  (SM) and  $f_{WW}/\Lambda^2 \neq 0$  in FIG. 11. We see the differences between the  $f_{WW}/\Lambda^2 \neq 0$  and the SM background distributions. The harder distributions for the signal motivate us to impose the following cuts

$$E_{W_{h1}} > 350 \text{ GeV}, \quad E_{W_{l1}} > 200 \text{ GeV}, \quad (36)$$

to effectively suppress the SM background. We next introduce the transverse momentum difference

$$\Delta P_T(W_{h1}W_{h2}) \equiv |\vec{P}_T(W_{h1}) - \vec{P}_T(W_{h2})|^2. \quad (37)$$

In FIG. 12, we plot this variable  $\Delta P_T(W_{h1}W_{h2})$  and the invariant mass  $M_{W_{h1}W_{h2}}$  of the higher  $P_T$   $W$ -pair for  $f_{WW}/\Lambda^2 = 1.5 \text{ TeV}^{-2}$  and  $f_{WW}/\Lambda^2 = 0$  (SM). We see that the cuts

$$\Delta P_T(W_{h1}W_{h2}) > 750 \text{ GeV}, \quad M_{W_{h1}W_{h2}} > 850 \text{ GeV}, \quad (38)$$

can help improve the signal to background ratio.

We now examine the transverse momentum and the rapidity distributions. Denote the larger and smaller absolute rapidities of  $W_{h1}$  and  $W_{h2}$  by  $y_>(W_h)$  and  $y_<(W_h)$ , respectively. FIGURE 13 shows the  $P_T(W_{h1})$  and  $y_>(W_h)$  distributions for  $f_{WW}/\Lambda^2 = 1.5 \text{ TeV}^{-2}$  and  $f_{WW}/\Lambda^2 = 0$  (SM). We see that the cuts

$$p_T(W_{h1}) > 400 \text{ GeV}, \quad |y_>(W_h)| < 1.2, \quad (39)$$

can further improve the signal to background ratio. FIGURE 14 plots the  $y_>(W_l)$  and  $y_<(W_l)$  distributions for the  $f_{WW}/\Lambda^2 = 1.5 \text{ TeV}^{-2}$  and  $f_{WW}/\Lambda^2 = 0$  (SM). We impose the following cuts

$$\text{both } |y_>(W_l)| \text{ and } |y_<(W_l)| < 2.0, \quad |y_>(W_l)| \text{ and/or } |y_<(W_l)| < 1.2. \quad (40)$$

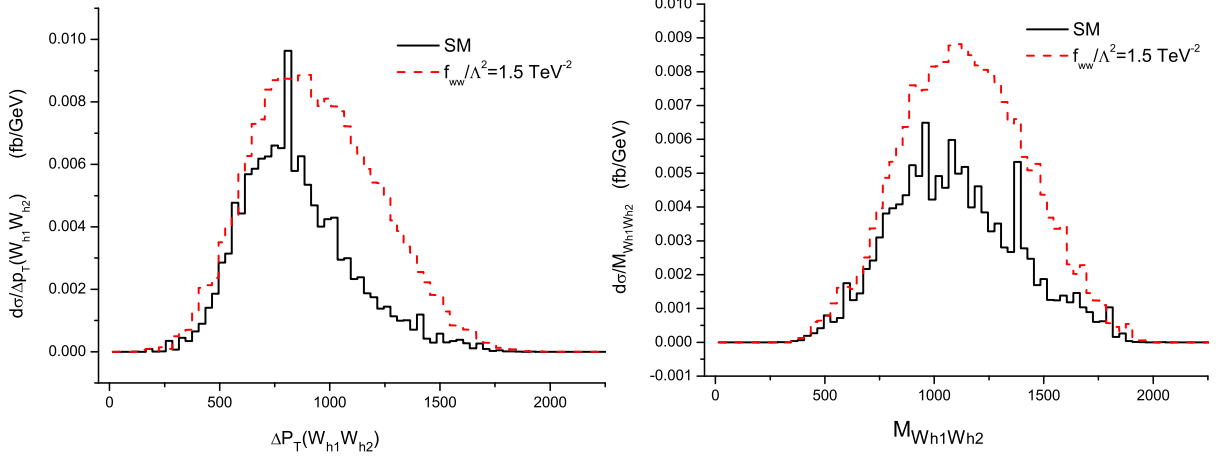


FIG. 12:  $\Delta P_T(W_{h1}W_{h2})$  and  $M_{W_{h1}W_{h2}}$  distributions of the  $f_{WW}/\Lambda^2 = 1.5 \text{ TeV}^{-2}$  and  $f_{WW}/\Lambda^2 = 0$  (SM).

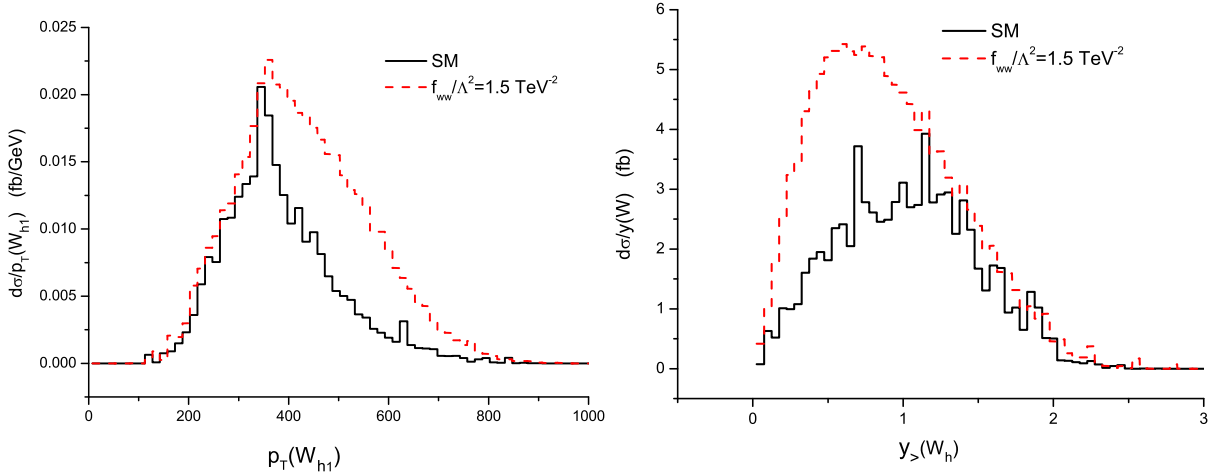


FIG. 13:  $P_T(W_{h1})$  and  $y_{>}(W_h)$  distributions of the  $f_{WW}/\Lambda^2 = 1.5 \text{ TeV}^{-2}$  and  $f_{WW}/\Lambda^2 = 0$  (SM).

Finally, we plot the  $p_T(W_{l2})$  and  $P_T(W_{l1})$  distributions for  $f_{WW}/\Lambda^2 = 1.5 \text{ TeV}^{-2}$  and  $f_{WW}/\Lambda^2 = 0$  (SM) in FIG. 15, which suggest the following optimal cuts

$$\text{both } P_T(W_{l2}) \text{ and } P_T(W_{l1}) > 100 \text{ GeV}, \quad P_T(W_{l2}) \text{ and/or } P_T(W_{l1}) > 250 \text{ GeV}. \quad (41)$$

With the imposed cuts (36) – (41), the SM background can be effectively suppressed. The ef-

TABLE III: Detection efficiencies after various cuts for  $f_{WW}/\Lambda^2 = 1.5 \text{ TeV}^{-2}$  as an example.

	no cuts	cut (36)	cuts (36)+(38)+(39)	cuts (36)+(38)+(39)+(40)+(41)
$\sigma_{\text{signal}}$ (fb)	3.2	2.8	1.3	1.0
$\sigma_{\text{bkgd}}$ (fb)	27	3.8	1.2	0.37
effectiveness $r$	-	87%/14% = 6.2	46%/31% = 1.5	78%/31% = 2.5

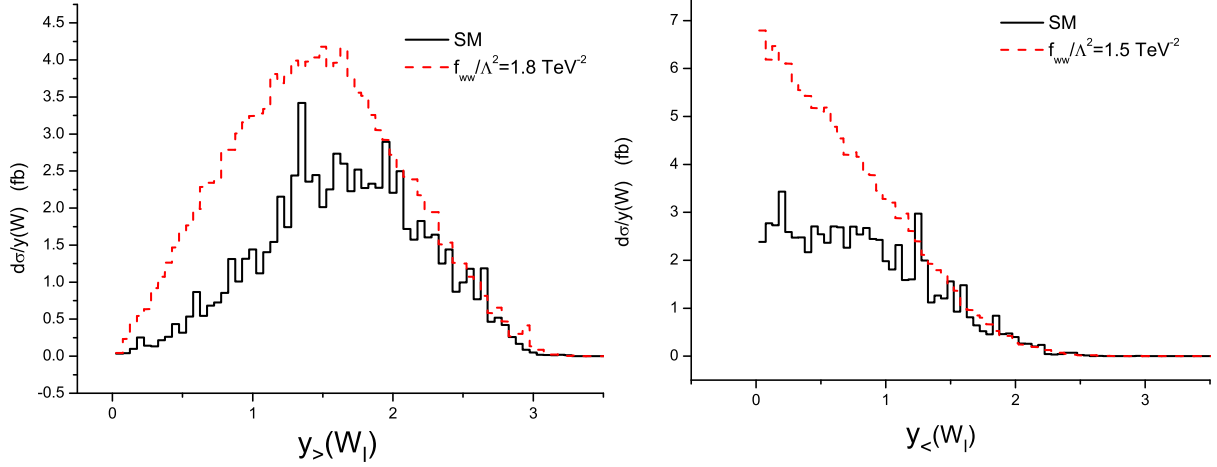


FIG. 14:  $y_>(W_l)$  and  $y_<(W_l)$  distributions of the  $f_{WW}/\Lambda^2 = 1.5 \text{ TeV}^{-2}$  and  $f_{WW}/\Lambda^2 = 0$  (SM).

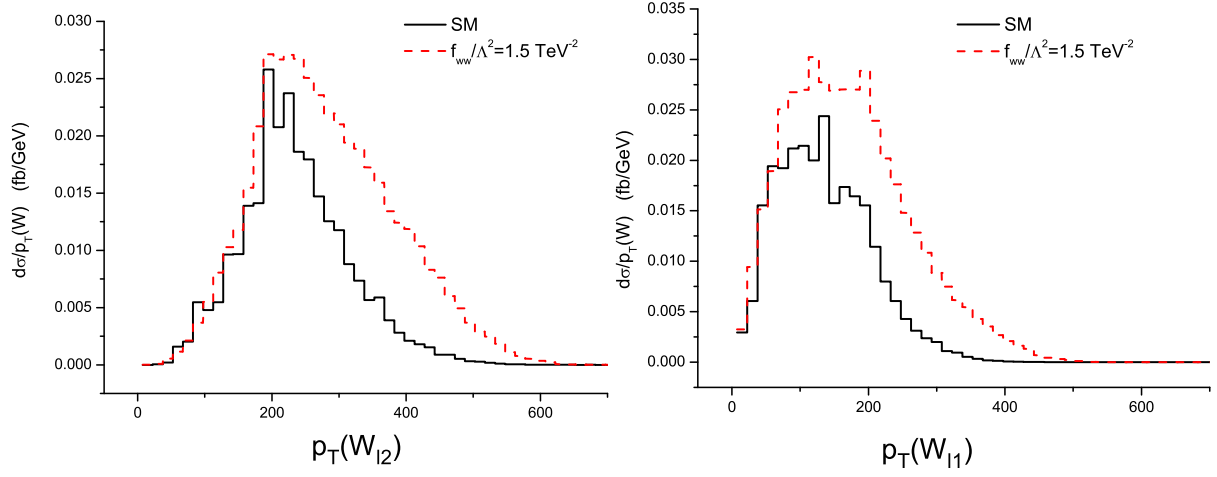


FIG. 15:  $P_T(W_{l2})$  and  $P_T(W_{l1})$  distributions of the  $f_{WW}/\Lambda^2 = 1.5 \text{ TeV}^{-2}$  and  $f_{WW}/\Lambda^2 = 0$  (SM).

fectiveness of Eq. (23) after imposing each of the cuts are shown in TABLE III. Again, taking into account the 50% safety factor in the final state  $W$  boson reconstruction by  $M_W$  from  $M_Z$ , we obtain the number of events for  $m_H = 115, 130, 200$  and  $300$  GeV at the polarized ( $2\lambda_e P_c = -1$ ) and unpolarized photon colliders based on the 3 TeV CLIC. The results for the cases of  $f_{WW}/\Lambda^2$  dominance are plotted in FIG. 16. The  $1\sigma$ ,  $2\sigma$ ,  $3\sigma$  and  $5\sigma$  statistical deviations  $\sigma_{stat}$  are shown by the bullets, squares, triangles and asterisks, respectively, along the  $f_{WW}/\Lambda^2$  axis. We see that, at the 3 TeV CLIC, the process  $\gamma\gamma \rightarrow WWWW$  can sensitively test  $f_{WW}/\Lambda^2$ . The sensitivity for  $m_H = 115, 130$  and  $200$  GeV is similar, while that for  $m_H = 300$  GeV is significantly better just as in the case of  $\gamma\gamma \rightarrow ZZ$ . From FIG. 16 we see that the  $2\sigma$  and  $3\sigma$  sensitivities for  $m_H = 115, 130$  and  $200$  GeV are roughly

$$\sqrt{s_{ee}} = 3 \text{ TeV polarized } (m_H = 115 - 200 \text{ GeV}) :$$

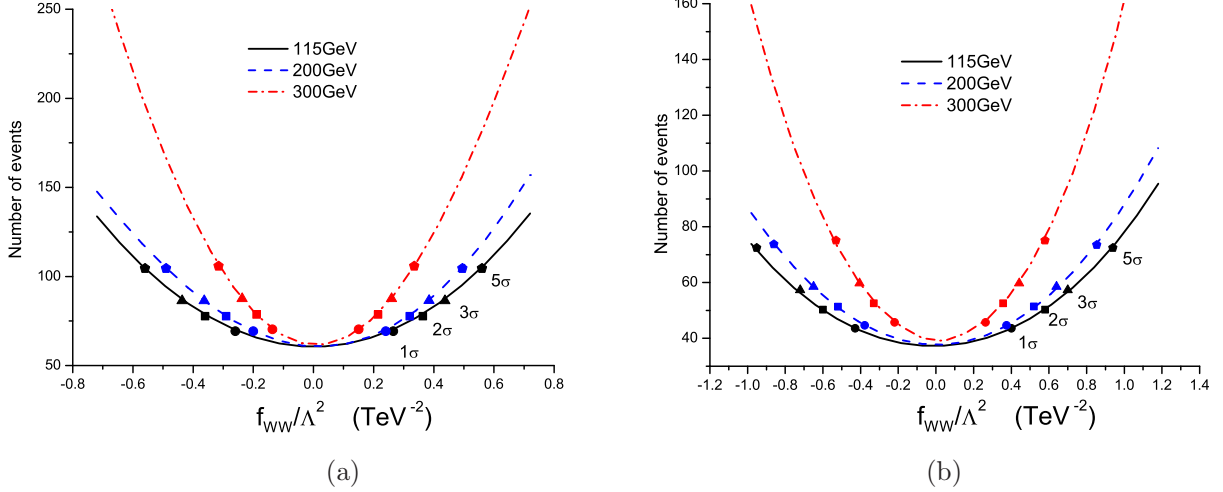


FIG. 16: Number of events of  $\gamma\gamma \rightarrow WWWW$  ( $W \rightarrow jj$ ) versus  $f_{WW}/\Lambda^2$  for  $m_H = 115, 200$  and  $300$  GeV at the  $\sqrt{s_{ee}} = 3$  TeV CLIC with the cuts (36)–(41) and taking account of the 50% safety factor for the final state  $W$  boson detection: (a) polarized, (b) unpolarized. The values of  $f_{WW}/\Lambda^2$  corresponding to  $1\sigma$ ,  $2\sigma$ ,  $3\sigma$  and  $5\sigma$  statistical deviations [cf. Eq. (19)] are shown on each curve by the bullets, squares, triangles and asterisks, respectively.

$$\begin{aligned}
2\sigma : \quad & -0.4 \text{ TeV}^{-2} < f_{WW}/\Lambda^2 < 0.4 \text{ TeV}^{-2}, \\
3\sigma : \quad & -0.45 \text{ TeV}^{-2} < f_{WW}/\Lambda^2 < 0.45 \text{ TeV}^{-2}, \\
\sqrt{s_{ee}} = 3 \text{ TeV unpolarized } (m_H = 115 - 200 \text{ GeV}) : \\
2\sigma : \quad & -0.6 \text{ TeV}^{-2} < f_{WW}/\Lambda^2 < 0.6 \text{ TeV}^{-2}, \\
3\sigma : \quad & -0.8 \text{ TeV}^{-2} < f_{WW}/\Lambda^2 < 0.8 \text{ TeV}^{-2}.
\end{aligned} \tag{42}$$

We note that although the sensitivities in the polarized and unpolarized cases are similar, they are about a factor of 6 and a factor of 3.6 more sensitive than the corresponding sensitivity  $|f_{WW}/\Lambda^2| \leq 2.9 \text{ TeV}^{-2}$  obtained from  $W^+W^+$  scattering at the LHC [12]. One can translate the above bounds into the corresponding sensitivities on  $g_{HVV}^{(i)}$ :

polarized :

$$\begin{aligned}
2\sigma : \quad & -0.005 \text{ TeV}^{-1} < g_{H\gamma\gamma} < 0.005 \text{ TeV}^{-1}, \\
& -0.011 \text{ TeV}^{-1} < g_{HWW}^{(1)} < 0.011 \text{ TeV}^{-1}, -0.021 \text{ TeV}^{-1} < g_{HWW}^{(2)} < 0.021 \text{ TeV}^{-1}, \\
& -0.011 \text{ TeV}^{-1} < g_{HZZ}^{(1)} < 0.011 \text{ TeV}^{-1}, -0.008 \text{ TeV}^{-1} < g_{HZZ}^{(2)} < 0.008 \text{ TeV}^{-1}, \\
& -0.006 \text{ TeV}^{-1} < g_{HZ\gamma}^{(1)} < 0.006 \text{ TeV}^{-1}, -0.004 \text{ TeV}^{-1} < g_{HZ\gamma}^{(2)} < 0.004 \text{ TeV}^{-1}, \\
3\sigma : \quad & -0.005 \text{ TeV}^{-1} < g_{H\gamma\gamma} < 0.005 \text{ TeV}^{-1}, \\
& -0.012 \text{ TeV}^{-1} < g_{HWW}^{(1)} < 0.012 \text{ TeV}^{-1}, -0.023 \text{ TeV}^{-1} < g_{HWW}^{(2)} < 0.023 \text{ TeV}^{-1},
\end{aligned}$$



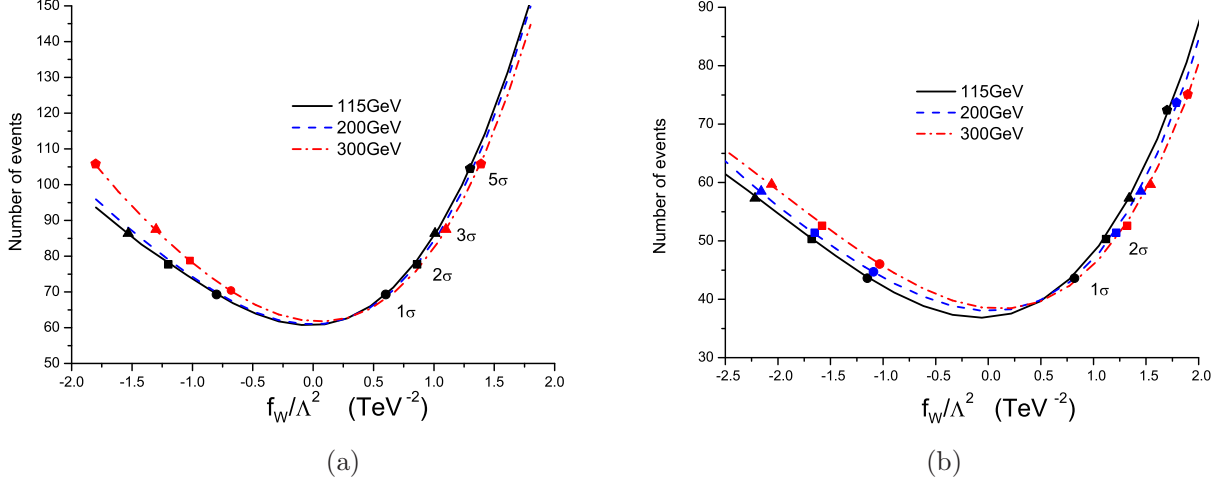


FIG. 17: Number of events of  $\gamma\gamma \rightarrow WWWW$  ( $W \rightarrow jj$ ) versus  $f_W/\Lambda^2$  for  $m_H = 115, 200$  and  $300$  GeV at the  $\sqrt{s_{ee}} = 3$  TeV CLIC with the cuts (36)–(41) and taking account of the 50% safety factor for the final state  $W$  boson detection: (a) polarized, (b) unpolarized. The values of  $f_W/\Lambda^2$  corresponding to  $1\sigma$ ,  $2\sigma$ ,  $3\sigma$  and  $5\sigma$  statistical deviations [cf. Eq. (19)] are shown on each curve by the bullets, squares, triangles and asterisks, respectively.

$$\begin{aligned}
-0.012 \text{ TeV}^{-1} < g_{HZZ}^{(1)} < 0.012 \text{ TeV}^{-1}, \quad -0.009 \text{ TeV}^{-1} < g_{HZZ}^{(2)} < 0.009 \text{ TeV}^{-1}, \\
-0.006 \text{ TeV}^{-1} < g_{HZ\gamma}^{(1)} < 0.006 \text{ TeV}^{-1}, \quad -0.005 \text{ TeV}^{-1} < g_{HZ\gamma}^{(2)} < 0.005 \text{ TeV}^{-1}. \quad (43)
\end{aligned}$$

unpolarized :

$$\begin{aligned}
2\sigma : \quad & -0.007 \text{ TeV}^{-1} < g_{H\gamma\gamma} < 0.007 \text{ TeV}^{-1}, \\
& -0.016 \text{ TeV}^{-1} < g_{HWW}^{(1)} < 0.016 \text{ TeV}^{-1}, \quad -0.031 \text{ TeV}^{-1} < g_{HWW}^{(2)} < 0.031 \text{ TeV}^{-1}, \\
& -0.016 \text{ TeV}^{-1} < g_{HZZ}^{(1)} < 0.016 \text{ TeV}^{-1}, \quad -0.012 \text{ TeV}^{-1} < g_{HZZ}^{(2)} < 0.012 \text{ TeV}^{-1}, \\
& -0.008 \text{ TeV}^{-1} < g_{HZ\gamma}^{(1)} < 0.008 \text{ TeV}^{-1}, \quad -0.007 \text{ TeV}^{-1} < g_{HZ\gamma}^{(2)} < 0.007 \text{ TeV}^{-1}, \\
3\sigma : \quad & -0.010 \text{ TeV}^{-1} < g_{H\gamma\gamma} < 0.010 \text{ TeV}^{-1}, \\
& -0.021 \text{ TeV}^{-1} < g_{HWW}^{(1)} < 0.021 \text{ TeV}^{-1}, \quad -0.042 \text{ TeV}^{-1} < g_{HWW}^{(2)} < 0.042 \text{ TeV}^{-1}, \\
& -0.021 \text{ TeV}^{-1} < g_{HZZ}^{(1)} < 0.021 \text{ TeV}^{-1}, \quad -0.016 \text{ TeV}^{-1} < g_{HZZ}^{(2)} < 0.016 \text{ TeV}^{-1}, \\
& -0.011 \text{ TeV}^{-1} < g_{HZ\gamma}^{(1)} < 0.011 \text{ TeV}^{-1}, \quad -0.008 \text{ TeV}^{-1} < g_{HZ\gamma}^{(2)} < 0.008 \text{ TeV}^{-1}. \quad (44)
\end{aligned}$$

The sensitivities in (43) and (44) are of the same order of magnitude but somewhat weaker than that for  $g_{H\gamma\gamma}$  in (30) and (33) as from the process  $\gamma\gamma \rightarrow ZZ$ . However, the process  $\gamma\gamma \rightarrow WWWW$  contains information of couplings  $g_{HVV}$ 's as seen in (43) and (44), thus the two processes are complementary. Compared with the sensitivity in (44), Eq. (43) with polarized beams improves the sensitivity by a factor of 1.5.

Next we look at the case of  $f_W/\Lambda^2$  dominance. As mentioned before, the contribution of FIG. 8(c) is negligible in this case, so that the signal rate is significantly smaller. Adopting the same cuts as given in Eqs. (36)–(41), the results are plotted in FIG. 17. We see that the asymmetry in the  $f_W/\Lambda^2 > 0$  and  $f_W/\Lambda^2 < 0$  regions due to the interference is more pronounced than that in the case of  $f_{WW}/\Lambda^2$  dominance (cf. FIG. 16). This is because that the SM background is more similar in size to the signal in the this case. Based on FIG. 17, we obtain the  $2\sigma$  and  $3\sigma$  bounds

$$\begin{aligned}
&\text{polarized :} \\
&\quad 2\sigma : \quad -1.2 \text{ TeV}^{-2} \leq f_W/\Lambda^2 \leq 0.8 \text{ TeV}^{-2}, \\
&\quad 3\sigma : \quad -1.6 \text{ TeV}^{-2} \leq f_W/\Lambda^2 \leq 1.1 \text{ TeV}^{-2}, \\
&\text{unpolarized :} \\
&\quad 2\sigma : \quad -1.5 \text{ TeV}^{-2} \leq f_W/\Lambda^2 \leq 1.2 \text{ TeV}^{-2}, \\
&\quad 3\sigma : \quad -2.4 \text{ TeV}^{-2} \leq f_W/\Lambda^2 \leq 1.5 \text{ TeV}^{-2}. \tag{45}
\end{aligned}$$

Compared with the  $3\sigma$  sensitivity obtained from  $W^+W^+$  scattering at the LHC [12], the present result in the polarized case is slightly improved, while that in the unpolarized case is a little less sensitive. As we have seen before, the sensitivity in the polarized case is a factor of 1.5 better with respect to the unpolarized case. The results again can be translated into sensitivities for  $g_{HVV}^{(i)}$ 's

$$\begin{aligned}
&\text{polarized :} \\
&\quad 2\sigma : \quad -0.031 \text{ TeV}^{-1} < g_{HWW}^{(1)} < 0.021 \text{ TeV}^{-1}, -0.042 \text{ TeV}^{-1} < g_{HWW}^{(2)} < 0.062 \text{ TeV}^{-1}, \\
&\quad \quad -0.031 \text{ TeV}^{-1} < g_{HZZ}^{(1)} < 0.021 \text{ TeV}^{-1}, \quad -0.016 \text{ TeV}^{-1} < g_{HZZ}^{(2)} < 0.024 \text{ TeV}^{-1}, \\
&\quad \quad -0.017 \text{ TeV}^{-1} < g_{HZ\gamma}^{(1)} < 0.011 \text{ TeV}^{-1}, \quad -0.009 \text{ TeV}^{-1} < g_{HZ\gamma}^{(2)} < 0.013 \text{ TeV}^{-1}, \\
&\quad 3\sigma : \quad -0.042 \text{ TeV}^{-1} < g_{HWW}^{(1)} < 0.029 \text{ TeV}^{-1}, -0.057 \text{ TeV}^{-1} < g_{HWW}^{(2)} < 0.083 \text{ TeV}^{-1}, \\
&\quad \quad -0.042 \text{ TeV}^{-1} < g_{HZZ}^{(1)} < 0.029 \text{ TeV}^{-1}, \quad -0.022 \text{ TeV}^{-1} < g_{HZZ}^{(2)} < 0.032 \text{ TeV}^{-1}, \\
&\quad \quad -0.022 \text{ TeV}^{-1} < g_{HZ\gamma}^{(1)} < 0.015 \text{ TeV}^{-1}, \quad -0.012 \text{ TeV}^{-1} < g_{HZ\gamma}^{(2)} < 0.018 \text{ TeV}^{-1}. \tag{46}
\end{aligned}$$

unpolarized :

$$\begin{aligned}
&\quad 2\sigma : \quad -0.039 \text{ TeV}^{-1} < g_{HWW}^{(1)} < 0.031 \text{ TeV}^{-1}, -0.062 \text{ TeV}^{-1} < g_{HWW}^{(2)} < 0.078 \text{ TeV}^{-1}, \\
&\quad \quad -0.039 \text{ TeV}^{-1} < g_{HZZ}^{(1)} < 0.031 \text{ TeV}^{-1}, \quad -0.024 \text{ TeV}^{-1} < g_{HZZ}^{(2)} < 0.030 \text{ TeV}^{-1}, \\
&\quad \quad -0.021 \text{ TeV}^{-1} < g_{HZ\gamma}^{(1)} < 0.017 \text{ TeV}^{-1}, \quad -0.013 \text{ TeV}^{-1} < g_{HZ\gamma}^{(2)} < 0.017 \text{ TeV}^{-1}, \\
&\quad 3\sigma : \quad -0.062 \text{ TeV}^{-1} < g_{HWW}^{(1)} < 0.039 \text{ TeV}^{-1}, -0.078 \text{ TeV}^{-1} < g_{HWW}^{(2)} < 0.12 \text{ TeV}^{-1},
\end{aligned}$$

TABLE IV: Summary of the  $3\sigma$  sensitivity for  $g_{H\gamma\gamma}$  (in  $\text{TeV}^{-1}$ ) from  $\gamma\gamma \rightarrow ZZ$  at various  $e^+e^-$  linear colliders compared with the corresponding sensitivity  $-0.036 < g_{H\gamma\gamma} < 0.036$  from  $W^+W^+ \rightarrow W^+W^+$  at the LHC [12].

$3\sigma$ sensitivity for $g_{H\gamma\gamma}$ from $\gamma\gamma \rightarrow ZZ$ at the LC
500 GeV ILC ( $m_H = 115 - 200$ GeV):
unpolarized: $-0.025 < g_{H\gamma\gamma} < 0.012$
polarized: $-0.022 < g_{H\gamma\gamma} < 0.0082$
1 TeV ILC ( $m_H = 115 - 300$ GeV):
unpolarized: $-0.0098 < g_{H\gamma\gamma} < 0.0073$
polarized: $-0.0073 < g_{H\gamma\gamma} < 0.0054$
3 TeV CLIC ( $m_H = 115 - 300$ GeV):
unpolarized: $-0.0022 < g_{H\gamma\gamma} < 0.0022$
polarized: $-0.0015 < g_{H\gamma\gamma} < 0.0015$

$$\begin{aligned}
-0.062 \text{ TeV}^{-1} < g_{HZZ}^{(1)} < 0.039 \text{ TeV}^{-1}, \quad -0.030 \text{ TeV}^{-1} < g_{HZZ}^{(2)} < 0.048 \text{ TeV}^{-1}, \\
-0.034 \text{ TeV}^{-1} < g_{HZ\gamma}^{(1)} < 0.021 \text{ TeV}^{-1}, \quad -0.026 \text{ TeV}^{-1} < g_{HZ\gamma}^{(2)} < 0.017 \text{ TeV}^{-1}.
\end{aligned} \quad (47)$$

In conclusion, the process  $\gamma\gamma \rightarrow WWWW$  at the 3 TeV CLIC can provide a rather sensitive test of  $g_{HVV}^{(i)}$  for the coupling  $f_{WW}/\Lambda^2$ , while it only provides a test of the coupling  $f_W/\Lambda^2$  with similar sensitivity to those obtained from  $W^+W^+$  scattering at the LHC [12].

## VI. SUMMARY

Once a light Higgs boson is discovered at the LHC and the ILC, an immediate question is whether it is the SM-like or not. Measuring the anomalous couplings of the Higgs boson may provide an answer. So far, the most sensitive way of measuring the anomalous gauge couplings of the Higgs boson at the LHC is via  $W^+W^+$  scattering [12]. In this paper, we have given a systematic study of the sensitivity of testing the anomalous gauge couplings  $g_{HVV}^{(i)}$ 's of the Higgs boson via  $\gamma\gamma \rightarrow ZZ$  and  $\gamma\gamma \rightarrow WWWW$  for a Higgs boson with  $m_H = 115 - 300$  GeV at polarized and unpolarized photon colliders based on  $e^+e^-$  linear colliders of various energies. We have developed certain kinematic cuts which can suppress the SM backgrounds effectively.

The process  $\gamma\gamma \rightarrow ZZ$  provides a sensitive test of the anomalous coupling  $g_{H\gamma\gamma}$ . The kinematic cuts we proposed are (20), (21) and (22), which effectively suppress the SM background. At the 500 GeV ILC, the obtained result shows that the testing sensitivities for  $m_H \leq 2M_W$  are all similar, while that of  $m_H = 300$  GeV is much higher due to the  $s$ -channel resonant production. At the 1 TeV ILC and the 3 TeV CLIC, the  $s$ -channel resonance effect is not so significant after imposing the cuts, and the sensitivities for  $m_H = 115 - 300$  GeV are all similar. The obtained number of events and the

TABLE V: Summary of the  $3\sigma$  testing sensitivities for  $g_{HVV}^{(i)}$ 's (in  $\text{TeV}^{-1}$ ) for  $m_H = 115 - 200$  GeV from  $\gamma\gamma \rightarrow WWWW$  at the 3 TeV CLIC compared with the corresponding sensitivity from  $W^+W^+ \rightarrow W^+W^+$  at the LHC (from Ref. [12]).

$3\sigma$ sensitivity for $g_{HVV}^{(i)}$ from $\gamma\gamma \rightarrow WWWW$ at the CLIC	$3\sigma$ sensitivity for $g_{HVV}^{(i)}$ at the LHC
$f_{WW}/\Lambda^2$ dominant: unpolarized: $ g_{H\gamma\gamma}  < 0.010$ , $ g_{HWW}^{(1)}  < 0.021$ , $ g_{HWW}^{(2)}  < 0.042$ $ g_{HZZ}^{(1)}  < 0.021$ , $ g_{HZZ}^{(2)}  < 0.016$ $ g_{Hz\gamma}^{(1)}  < 0.011$ , $ g_{Hz\gamma}^{(2)}  < 0.008$ polarized: $ g_{H\gamma\gamma}  < 0.005$ $ g_{HWW}^{(1)}  < 0.012$ , $ g_{HWW}^{(2)}  < 0.023$ $ g_{HZZ}^{(1)}  < 0.012$ , $ g_{HZZ}^{(2)}  < 0.009$ $ g_{Hz\gamma}^{(1)}  < 0.006$ , $ g_{Hz\gamma}^{(2)}  < 0.005$	$f_{WW}/\Lambda^2$ dominant: $ g_{H\gamma\gamma}  < 0.035$ , $ g_{HWW}^{(1)}  < 0.075$ , $ g_{HWW}^{(2)}  < 0.15$ $ g_{HZZ}^{(1)}  < 0.075$ , $ g_{HZZ}^{(2)}  < 0.058$ $ g_{Hz\gamma}^{(1)}  < 0.041$ , $ g_{Hz\gamma}^{(2)}  < 0.032$
$f_W/\Lambda^2$ dominant: unpolarized: $-0.062 < g_{HWW}^{(1)} < 0.039$ , $-0.078 < g_{HWW}^{(2)} < 0.12$ $-0.62 < g_{HZZ}^{(1)} < 0.039$ , $-0.030 < g_{HZZ}^{(2)} < 0.048$ $-0.034 < g_{Hz\gamma}^{(1)} < 0.021$ , $-0.026 < g_{Hz\gamma}^{(2)} < 0.017$ polarized: $-0.042 < g_{HWW}^{(1)} < 0.029$ , $-0.057 < g_{HWW}^{(2)} < 0.083$ $-0.042 < g_{HZZ}^{(1)} < 0.029$ , $-0.022 < g_{HZZ}^{(2)} < 0.032$ $-0.022 < g_{Hz\gamma}^{(1)} < 0.015$ , $-0.012 < g_{Hz\gamma}^{(2)} < 0.018$	$f_W/\Lambda^2$ dominant: $-0.047 < g_{HWW}^{(1)} < 0.042$ , $-0.083 < g_{HWW}^{(2)} < 0.094$ $-0.047 < g_{HZZ}^{(1)} < 0.042$ , $-0.032 < g_{HZZ}^{(2)} < 0.036$ $-0.025 < g_{Hz\gamma}^{(1)} < 0.022$ , $-0.018 < g_{Hz\gamma}^{(2)} < 0.020$

statistic deviations are shown in FIGs. 5–7. We summarize the obtained testing sensitivities [cf. (25), (29), (30), (31), (32), and (33)] in TABLE IV together with the corresponding sensitivity obtained from  $W^+W^+$  scattering at the LHC for comparison. For  $m_H = 300$  GeV at the 500 GeV ILC, the  $5\sigma$  sensitivity is [cf. Eq. (27)]

$$-0.0013 \text{ TeV}^{-1} < g_{H\gamma\gamma} < 0.0085 \text{ TeV}^{-1}. \quad (48)$$

If one can tune the energy of the ILC, it will be optimal to make  $E_{\gamma\gamma}$  peak at the resonant energy. For instance, for  $m_H = 300$  GeV, we can tune the  $e^+e^-$  energy to  $\sqrt{s_{ee}} = 380$  GeV to have  $E_{\gamma\gamma}$  to peak at 300 GeV. In this case, the  $5\sigma$  sensitivity is [cf. Eq. (28)]

$$-0.00012 \text{ TeV}^{-1} < g_{H\gamma\gamma} < 0.00030 \text{ TeV}^{-1}. \quad (49)$$

As for the process  $\gamma\gamma \rightarrow WWWW$ , the 500 GeV and 1 TeV ILC cannot deliver large enough signal rates due to phase space suppression. At the 3 TeV CLIC however, the  $\gamma\gamma \rightarrow WWWW$  process becomes interesting. We have also developed certain kinematic cuts to suppress the SM background [cf. (36)–(41)]. The obtained number of events and the statistic deviations are shown in FIGs. 16 and 17.

We summarize the obtained  $3\sigma$  testing sensitivities [cf. (43), (44), (46), and (47)] in TABLE V together with the corresponding sensitivities obtained from  $W^+W^+$  scattering at the LHC for comparison.

We have presented our results with an integrated luminosity of  $1 \text{ ab}^{-1}$ , and the sensitivities are obtained by statistical errors only. We found that the beam polarization is beneficial to the search. The polarized photon colliders can improve the sensitivities by roughly a factor of 1.2–1.4 for  $\gamma\gamma \rightarrow ZZ$  and a factor of 1.5 for  $\gamma\gamma \rightarrow WWWW$  relative to the unpolarized photon colliders.

In conclusion, photon colliders based on  $e^+e^-$  linear colliders can provide more sensitive tests of the anomalous gauge couplings of the Higgs boson than the LHC does. If a Higgs boson candidate is found at the LHC, then linear colliders can give a better answer to whether the Higgs boson is SM-like or not. In the absence of new particle observation beyond a light Higgs boson, testing anomalous Higgs boson couplings may provide a way of discovering the effect of new physics beyond the SM.

## ACKNOWLEDGMENT

This work is supported by National Natural Science Foundation of China under Grant No. 90403017 (YPK and BZ) and No. 10435040 (BZ), and by U.S. DOE under Grant No. DE-FG02-95ER40896 and Wisconsin Alumni Research Foundation (TH).

- 
- [1] S. Eidelman *et al.* (Particle Data Group), Phys. Lett. B **592**, 1 (2004); LEP Electroweak Working Group, <http://lepewwg.web.cern.ch/LEPEWWG/> for updated information.
  - [2] C. Diaconu, Talk given at the 2005 international Symposium on Lepton Photon Interactions at High Energy, Upsalla, Sweden, hep-ex/0510035; A. Sopczak, talk presented at the workshop *Collider Physics: From the Tevatron to the LHC to the Linear Collider*, the Aspen Center for Physics, summer 2005.
  - [3] ATLAS Technical Design Report, CERN-LHCC-94-43; CMS Technical Design Report, CERN-LHCC-94-38.
  - [4] J.A. Aguilar-Saavedra *et al.*, ECFA/DESY LC Physics Working Group Collaboration, DESY 2001-011 and arXiv:hep-ph/0106315; T. Abe *et al.*, American LC Working Group Collaboration, arXiv:hep-ex/0106055; K. Abe *et al.*, ACFA LC Working Group Collaboration, arXiv:hep-ex/0109166.
  - [5] L. Susskind, Phys. Rev. D **20**, 2619 (1979); G. 'tHooft, in *Recent Development in Gauge Theories*, edited by G. 'tHooft *et al.* (Plenum, New York, 1979).
  - [6] W. Buchmüller and D. Wyler, Nucl. Phys. **B268**, 621 (1986); C. J. C. Burgess and H. J. Schnitzer, Nucl. Phys. **B228**, 454 (1983); C. N. Leung, S. T. Love and S. Rao, Z. Phys. **31**, 433 (1986).
  - [7] A. De Rújula, M. B. Gavela, P. Hernández and E. Massó, Nucl. Phys. **B384**, 3 (1992); K. Hagiwara, S. Ishihara, R. Szalapski, and D. Zeppenfeld, Phys. Rev. D **48**, 2182 (1993).
  - [8] O.J.P. Eboli, M.C. Gonzalez-Garcia, S.M. Lietti, and S.F. Novaes, Phys. Lett. B **478**, 199 (2000).
  - [9] F. de Campos, M.C. Gonzalez-Garcia, S.M. Lietti, S.F. Novaes, and R. Rosenfeld, Phys. Lett. B **435**, 407 (1998).

- [10] D. Zeppenfeld, hep-ph/0203123; T. Plehn, D. Rainwater, and D. Zeppenfeld, Phys. Rev. Lett. **88**, 0510801 (2002).
- [11] H.-J. He, Y.-P. Kuang, C.-P. Yuan, and B. Zhang, Phys. Lett. B **554**, 64 (2003).
- [12] B. Zhang, Y.-P. Kuang, H.-J. He, and C.-P. Yuan, Phys. Rev. D **67**, 114024 (2003).
- [13] V. Barger, K. Cheung, A. Djouadi, B.A. Kniel, and P. M. Zerwas, Phys. Rev. D **49**, 79 (1994); M. Kramer, J. Kuhn, M. L. Stong and P. M. Zerwas, Z. Phys. C **64**, 21 (1994); K. Hagiwara and M. Stong, Z. Phys. C **62**, 99 (1994); J.F. Gunion, T. Han, and R. Sobey, Phys. Lett. B **429**, 79 (1995); K. Hagiwara, S. Ishihara, J. Kamoshita, and B.A. Kniehl, Eur. Phys. J. **14**, 457 (2000).
- [14] V. Barger, T. Han, P. Langacker, B. McElrath, and P.M. Zerwas, Phys. Rev. **D67**, 115001 (2003) [hep-ph/0301097].
- [15] For a review on collider phenomenology, M. C. Gonzalea-Garcia, Int. J. Mod. Phys. A **14**, 3121 (1999).
- [16] M. E. Peskin and T. Takeuchi, Phys. Rev. Lett. **65**, 964 (1990).
- [17] G.J. Gounaris, J. Layssac, and F.M. Renard, Phys. Lett. B **332**, 146 (1994); G.J. Gounaris, J. Layssac, J.E. Pascalis, and F.M. Renard, Z. Phys. C **66**, 619 (1995).
- [18] O. J. P. Eboli, et al., Phys. Rev. D **47**, 1889(1993); Kingman Cheung, Phys. Rev. D **47**, 3750 (1993).
- [19] G. Moortgat-Pick *et al.*, SLAC-PUB-1087, CERN-PH-TH-2005-036, DESY-05-059, FERMILAB-PUB-05-060-T, IPPP-04-50, KEK-2005-16, PRL-TH-05-06, SHEP-05-03, hep-ph/0507011.
- [20] I.F.Ginzburg, G.L. Kotkin, S.L. Panfil, V.G. Serbo, and V.I. Telnov, Nucl. Instr. and Methods in Phys. Res. **219**, 5 (1984); B. Badelek *et al.*, Int. J. Mod. Phys. A **19**, 5097 (2004) (Part VI of TESLA Technical Design Report, DESY 2001-011).
- [21] Part VI of TESLA Technical Design Report, DESY Report No. 2001-011, 2001.
- [22] Part I of TESLA Technical Design Report, DESY Report No. 2001-011, 2001.
- [23] M. Battaglia et al., hep-ph/0412251.
- [24] M.S. Berger and M.S. Chanowitz, Nucl. Instrum. Meth. A **355**, 52 (1995).
- [25] G. Jikia, Nucl. Phys. **B405**, 24 (1993).
- [26] J.M. Cornwall, D.N. Levin, and G. Tiktopoulos, Phys. Rev. D **10**, 1145 (1974); C.E.Vayonakis, Lett. Nuovo Cimento **17**, 383 (1976); B.W. Lee, C. Quigg, and H. Thacher, Phys. Rev. D **16**, 1519 (1977); M.S. Chanowitz and M.K. Gaillard, Nucl. Phys. **B261**, 379 (1985); G.J. Gounaris, R. Kögerler, and H. Neufeld, Phys. Rev. D **34**, 3257 (1986); H. Veltman, *ibid.* **41**, 2294 (1990); W.B. Kilgore, Phys. Lett. B **294**, 257 (1988); Y.-P. Yao and C.-P. Yuan, Phys. Rev. D **38**, 2237 (1988); J. Bagger and C. Schmidt, *ibid.* **41**, 264 (1990); H.-J. He, Y.-P. Kuang, and X. Li, Phys. Rev. Lett. **69**, 2619 (1992); Phys. Rev. D **49**, 4842 (1994); Phys. Lett. B **329**, 278 (1994); H.-J. He and W.B. Kilgore, Phys. Rev. D **55**, 1515 (1997).
- [27] The ability of distinguishing the final state  $Z$  from  $W$  in the dijet mode has been considered in the design of the the large size detector for the ILC. For example, R. Pöschl, lectures given at 2005 International Workshop/Summer School on Physics/Detector/Accelerator at the linear collider, July 15–20, Tsinghua University, Beijing, China.
- [28] S. Brodsky, in *Proceedings of Workshop on Physics and Experiments with Linear  $e^+e^-$  Colliders*, Waikoloa, Hawaii, edited by F. Harris (World Scientific, Singapore).
- [29] K. Cheung, Phys. Lett. B **323**, 85 (1994).
- [30] K. Cheung, Phys. Rev. D **50**, 4290 (1994).
- [31] K. Abe *et al.*, Particle Physics Experiments at JLC, KEK Report 2001-11.